

QUEEN'S UNIVERSITY BELFAST

MSCI THESIS

**Laser Wakefield Accelerator Simulations
Using EPOCH**

Author:
Aaron O'Neill

Supervisor:
Dr. Gianluca Sarri

*A thesis submitted in fulfillment of the requirements
for the degree of Master in Science
in the*

School of Mathematics and Physics

March 20, 2017

Abstract

Laser wakefield accelerators (LWFA) provide a cheap, compact and accessible form of electron acceleration. These systems use high intensity laser pulses to drive a large amplitude plasma density wake. This wake is then used to trap and accelerate electrons to high energies. This particle acceleration technique still requires considerable research in order to produce the high quality particle bunch associated with conventional RF accelerators. Fine control of plasma parameters will allow some of the limitations of this method to be overcome or suppressed. Theoretical considerations show that there are several limiting factors including laser diffraction in the plasma, electron dephasing and pump depletion. Here, each of the limitations is considered and a method of reducing their effects proposed. The consequences of pulse length variation in producing ideally formed wakefield structures is first investigated for three different pulse lengths. Each of these pulse lengths was simulated for Gaussian and square pulse envelope profiles. A method to inject electrons into the accelerating region of the plasma density wave using varying concentrations of Nitrogen neutrals is introduced and finally a focussing beam method is developed and used to demonstrate the detrimental effects of a rapidly focussing pulse. Each of the systems were simulated using a particle in cell code (EPOCH). There existed a resonance condition at which a stable bubble was formed, $L = \lambda_p$ and the Gaussian profile formed the most complete blow out regime. The introduction of Nitrogen neutrals greatly increased the number of electrons trapped and accelerated. The highest energy achieved over a distance of 1mm was 265MeV in $n_N = 5 \times 10^{16} \text{ cm}^{-3}$. The rapidly focussing pulse demonstrated that trapping and blow out would form more quickly for the focussing pulse but after the focal length the electron dephasing and diffraction effects were more severe than for the collimated beam. The Nitrogen injection technique was found to work very well but does require further investigation in order to find the optimal injection and acceleration. This combined with the pulse length resonance condition would provide the ideal basis for a high energy accelerator. Using a slowly focussing drive pulse through the injection set up would produce a coherent high energy bunch of electrons after 1mm with an energy in the range of 100 – 200MeV. This bunch could then be used to inject into a second high energy stage to accelerate the electrons to GeV energies.

Contents

1	Introduction	3
1.1	Plasma Physics	3
1.2	Acceleration in Plasma	6
1.3	Non-Linear Effects and Laser Plasma Interactions	6
1.3.1	The Ponderomotive Force	7
1.4	Laser Wakefield	8
1.4.1	Limits of Acceleration	8
1.5	Particle in Cell Code	10
1.5.1	EPOCH	11
1.6	Testing the Code	14
2	Pulse Length Variation	17
2.1	Methods	17
2.2	Results	18
2.2.1	Square Pulse	18
2.2.2	Gaussian Pulse	20
2.2.3	Electric Field for $L = \lambda_p$	22
2.3	Discussion	24
3	Injection Methods, Nitrogen Trapping	25
3.1	Methods	26
3.2	Results	27
3.2.1	0% - 10% Nitrogen ($n_{He} = 5 \times 10^{18} \text{ cm}^{-3}$)	27
3.2.2	Reduced Density ($n_{He} = 1 \times 10^{18} \text{ cm}^{-3}$)	38
3.3	Discussion	41
4	Focussing Beam	42
4.1	Methods	43
4.2	Results	44
4.3	Discussion	50
5	Discussion and Conclusions	51
6	Appendix	53
6.1	Input Decks	53
6.1.1	Two Stream Instability	53
6.1.2	Pulse Length Variation	53
6.1.3	Nitrogen Concentration	54
6.1.4	Focussing Beam	55
6.2	Tables	57
6.2.1	Nitrogen Trapping ($n_{He} = 5 \times 10^{18} \text{ cm}^{-3}$)	57
6.2.2	$n_{He} = 5 \times 10^{18} \text{ cm}^{-3}$ Peak Energy	57

1 Introduction

Plasma based electron accelerators have become the focus of a concentrated global research effort which, among many objectives, aims to produce high energy electron bunches using the interaction of very high intensity laser fields with a plasma. These plasma based accelerators were proposed in 1979 by Tajima and Dawson and it is only in recent years that the technological capability to implement these accelerators has become available. This technology has several practical advantages over the much larger conventional accelerators like LINACS (linear accelerators) and synchrotrons. The first being the physical size, by comparison the largest component of the laser wakefield accelerator is the laser system and these are tens of meters long (the actual acceleration length for wakefield, after the laser, is on the order of centimetres due to the huge acceleration gradients) in contrast to the kilometres long conventional systems. The difference in scale also means that the plasma based accelerator is not only more compact than the conventional technology but also considerably cheaper to run. The promise of cheap, compact and high energy electron acceleration is the primary motivation to study this phenomenon. In this discussion the mechanism of Laser Wakefield Accelerators will primarily be investigated.

1.1 Plasma Physics

Before discussing the more complex interactions of high intensity laser fields with a plasma as a means to accelerate electrons the principles of plasma physics must be introduced. Plasma in the simplest term is a fully ionised charged gas that is comprised of two fluids. A fluid of rapidly moving free electrons and a second fluid populated by the more slowly moving nuclei. It is worth noting that the term 'slowly moving' is relative only to the electron fluid and the nuclei will still have a considerable thermal velocity at the temperatures necessary to fully ionise even the lightest atoms.

This complete ionisation of all the atoms is the ideal situation for a plasma but is not always the case and there is likely to be some portion of neutral atoms or atoms that are not completely ionised. This may be due to recombination of the electrons with the nuclei or there simply not being enough energy to remove all the electrons from an atom in the first place and hence there will be a range of ionisation fractions. Even in a room temperature neutral gas there will be a very small number of ions present. This ionisation fraction in thermal equilibrium is described by the Saha equation [2];

$$\frac{n_i}{n_n} \approx 2.4 \times 10^{21} \frac{T^{\frac{3}{2}}}{n_i} e^{-\frac{U_i}{k_B T}} \quad (1)$$

Where T describes the gas temperature in Kelvin, n_i represents the number density of ions and n_n the number density of neutrals. The exponential term describes the effect of the energy ratio between the ionisation energy of the gas (U_i) and the thermal energy ($k_B T$). It can be seen that once the thermal energy of the gas is of the same order as the ionisation energy that the ionisation fraction will increase sharply but while below this threshold the ionisation fraction will remain small (10^{-122} for room temperature air [2]).

What conditions then differentiate a plasma from an ionised gas? Firstly a plasma must demonstrate quasi neutrality, that is, appear neutral over a certain scale length. This is most easily understood by stating the condition as $n_e \approx Z n_{ion}$, i.e. positive and negative charges balance and give the appearance of neutrality. Even with the condition of quasi-neutrality the Coulomb interactions will play a prominent role in the particle motions. In the kinetic theory of neutral gases one of the assumptions is that there should be no action at a distance so all the properties of such a gas are determined by direct collision. In a plasma collective effects arise due to the Coulomb action having the ability to act at a distance.

These conditions can be understood mathematically by considering how a plasma will react to the introduction of a test charge. Now that the Coulomb interplay has an effect, the introduction of the test charge will perturb the distribution of charge and disrupt quasi-neutrality in the local environment. For example in the presence of a positive charge imbalance the electron fluid will act to shield the charge and re-establish the local neutrality. Solving Poisson's equation for the electron distribution

(this result also assumes that the ions are stationary over the time-scale of the electron motions) gives a characteristic length known as the Debye length. This is the distance over which the effects of an introduced charge will be screened by the surrounding charges.

$$\lambda_D = \sqrt{\frac{\epsilon_0 k_B T}{ne^2}} \quad (2)$$

Where T is the temperature, ϵ_0 is the permittivity of free space, k_B the Boltzmann constant, e the elementary charge and n is the number density of electrons present. With the definition of this length a volume known as the Debye sphere can be defined as the sphere with radius λ_D . Now by simple multiplication of the volume of the Debye sphere and the number density of particles the number of particles in the sphere may be calculated (N_D).

These two quantities allow a set of mathematical conditions to be noted which represent the aforementioned qualities of a plasma.

$$\lambda_D \ll L \quad (3)$$

The Debye length must be greater than the scale length of the plasma to ensure that quasi-neutrality is possible.

$$N_D \gg 1 \quad (4)$$

There must be a large number of particles in the Debye sphere so that the charge density is high enough for collective behaviour to be present. This condition more specifically applies to a collisionless plasma

A third condition may be included for clarity;

$$\omega_p > \omega_c \quad (5)$$

The plasma frequency (ω_p) must be greater than the collisional frequency (ω_c) between species, plasma oscillations must dominate. This also applies to a collisionless plasma and is another way of writing condition 4.

The plasma state as defined by the above conditions is a complex system of free electrons and fully or partially ionised nuclei all moving with large velocities. The system and so the equation of motion that would describe the plasma must account for the electric and magnetic fields generated within the system (due to the motions of free charges) as well as the effects any externally applied field will have. As mentioned previously the plasma can be represented as two fluids, the electron fluid and the ion fluid. This allows the use of fluid equations modified to account for the plasma parameters. A common simplification is to assume that the ions are stationary from the perspective of the electrons and do not react on the time scales of the electron motion.

The equation of motion for a single particle can be written as a force balance between Newton's second law and the Lorentz force on a charged particle in the form;

$$m \frac{d\mathbf{v}}{dt} = e(\mathbf{E} + \mathbf{v} \times \mathbf{B}) \quad (6)$$

The plasma consists of many particles and this must be accounted for along with the fluid dynamics of the particles. To do this a Lagrangian Convective derivative is applied [2].

$$\frac{dG(x, t)}{dt} = \frac{\partial G}{\partial t} + \frac{\partial G}{\partial x} \frac{dx}{dt} \quad (7)$$

This derivative determines how a physical quantity ($G(x, t)$) of an element of fluid will evolve in time and space. Put simply it is the change seen if one were to be moving in and with an element of fluid. This differs from the Eulerian perspective in which the view is of a stationary element through which fluid moves. For a full treatment of fluid mechanics see Batchelor 'An Introduction to Fluid Dynamics' [3].

To model the plasma and produce a conservation of momentum equation that will predict motions the convective derivative must be applied to the single particle equation of motion. The physical quantity associated with the fluid is its velocity, $G(x, t) = v(x, t)$. Now equation 8 is obtained. The number density of particles, n , accounts for the many particles in the system and q represents the charge associated with the particles in the fluid.

$$mn \left[\frac{\partial \mathbf{v}}{\partial t} + (\mathbf{v} \cdot \nabla) \mathbf{v} \right] = nq(\mathbf{E} + \mathbf{v} \times \mathbf{B}) + \mathbf{F} \quad (8)$$

The force term on the right hand side of the conservation of momentum expression is comprised of two components.

$$\mathbf{F} = \mathbf{F}_{\text{int}} + \mathbf{F}_p \quad (9)$$

The first term, \mathbf{F}_{int} describes the exchange of momentum within the fluid due to collisions with the same species. If the plasma is considered to be collisionless, this is effectively true when the plasma is hot enough as the collisional frequency is inversely proportional to temperature, then $\mathbf{F}_{\text{int}} = 0$. The second term, \mathbf{F}_p , accounts for the exchange of momentum between fluids and so is effectively a pressure gradient.

To further increase the number of tools available to analyse the system a continuity equation is also included. This is a means of prohibiting particle creation in a volume. The rate of change of particles in a volume equals the number of particles flowing across the surface of the same volume, mathematically;

$$\frac{\partial n}{\partial t} + \nabla \cdot (n\mathbf{v}) = 0 \quad (10)$$

Now insofar as the calculation of plasma properties is concerned we have an equation describing the conservation of momentum (8) and an equation describing the conservation of mass (10). The electric and magnetic field effects still need to be accounted for and Maxwell's equations are used.

$$\nabla \cdot \mathbf{E} = \frac{\rho}{\epsilon_0} \quad (11)$$

$$\nabla \cdot \mathbf{B} = 0 \quad (12)$$

$$\nabla \times \mathbf{E} = -\frac{\partial \mathbf{B}}{\partial t} \quad (13)$$

$$\nabla \times \mathbf{B} = \mu_0 \mathbf{J} + \mu_0 \epsilon_0 \frac{\partial \mathbf{E}}{\partial t} \quad (14)$$

For a brief but informative guide to these equations see 'A Students Guide to Maxwell's Equations' D. Fleisch [4].

Maxwell's equations can be used to produce other expressions which will greatly increase the number of tools available to describe the physics of the system. Combining 13 and 14, and using a vector identity allows the definition of an electromagnetic wave equation.

$$\nabla^2 \mathbf{E} - \frac{1}{c^2} \frac{\partial^2 \mathbf{E}}{\partial t^2} - \mu_0 \frac{\partial \mathbf{J}}{\partial t} = 0 \quad (15)$$

These equations will enable the calculation of plasma properties in a wide variety of cases and conditions. This theoretical set up does, however, have it's limitations in that it will generally only apply to 'cold' non-relativistic plasma but it does give an insight into the plasma state and is an excellent starting point to move onto more complex systems.

An important result obtained from the consideration of the above equations, after some simplifying conditions, is the presence of a number density dependent plasma frequency.

$$\omega_p = \sqrt{\frac{n_0 e^2}{\epsilon_0 m_e}} \quad (16)$$

or in short hand calculation form [5];

$$\omega_p = 5.64 \times 10^4 \sqrt{n_0} \quad (17)$$

This is the natural frequency at which the electrons in the plasma (at a number density of n_0) will oscillate, suggesting a frequency at which resonance is attained.

From this description of the plasma frequency a plasma wave length may also be defined.

$$\lambda_p = \frac{2\pi c}{\omega_p} \quad (18)$$

1.2 Acceleration in Plasma

One of the major advantages of plasma based acceleration is that the plasma is able to sustain enormous electric fields. These fields are much larger than the fields produced in conventional RF linear accelerators. The fields in these solid state machines are limited by the break down voltage of the material they are built from (currently limited to 100MV m^{-1} [1]).

Further analysis of the equations discussed in section 1.1 shows that a fully ionised plasma can sustain electric fields in excess of,

$$E_0 = \frac{cm_e\omega_p}{e} \quad (19)$$

This is the cold non relativistic wave breaking formula obtained by one of the chief pioneers of the field, Dawson (1959) [6]. This, like most of the plasma expressions, may be written in a short hand calculation form.

$$E_0(\text{V m}^{-1}) \simeq 96\sqrt{n_0(\text{cm}^{-3})} \quad (20)$$

This small but powerful formula reveals the power that may be harnessed in the potential gradients of a plasma. With such high electric field values electrons may be accelerated to very high energies over short distances (on the sub centimetre scale). An experiment by Malka et al. in 2002 demonstrated that after focussing a high intensity laser through a gas jet electrons with an energy greater than 200MeV were observed [7].

The effect has been observed and so far theory has been considered which has the ability to describe particle motions in the plasma state (in the cold non-relativistic case). So how exactly can these large electric field strengths be utilised to accelerate particles? Diagnostic calculations etc have been obtained by a process of linearisation, that is, perturbing the plasma and considering only the first order perturbations to the system thereafter. These disturbances, for example an electric field displacing an electron from equilibrium, can have a strong effect on the plasma. In the case of displaced electrons a plasma density wave may propagate and this will induce regions of net electric field. This suggests a possible mechanism to carry the necessary accelerating electric field through the plasma in the form of density perturbations.

The principle mechanism behind the electron acceleration is that of the laser-plasma interaction. The nature of this interaction and more specifically the way in which an electron will behave in an intense laser field is discussed in the next section.

1.3 Non-Linear Effects and Laser Plasma Interactions

As mentioned the treatment up to this point has involved the first order terms of any perturbation applied to the plasma, however, some very interesting phenomena arise once the second order terms are included and worked through the equations.

First consider how an electron will move in the presence of an oscillating electric field. Assume a linearly plane polarised electromagnetic wave and consider the \mathbf{E} , and \mathbf{B} field components associated with such a wave. The motion of a charged particle in an electric and or magnetic field is described by the Lorentz force equation which is $\mathbf{F} = -e(\mathbf{E} + \mathbf{v} \times \mathbf{B})$ for an electron. If the magnetic field component

of this equation is small then the electric field will dominate. This electric field is sinusoidal in for the linear wave assumed and so the electron will simply oscillate with the electric field through it's equilibrium position. The motion becomes slightly more complex once the velocity of the electron becomes relativistic. At such intensities the \mathbf{B} field component becomes comparable to the electric field and hence the $\mathbf{v} \times \mathbf{B}$ term is significant and causes a force in the direction of propagation.

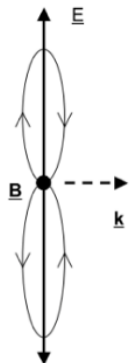


Figure 1: *The figure of eight type motion that an electron will exhibit in a relativistically intense laser field. The magnetic field dependent component of the Lorentz force will cause the electron to be accelerated in the direction of propagation, \mathbf{k} , twice per laser cycle. [2]*

The second way of writing the laser strength parameter, equation 21, in plain terms is the transverse momentum imparted to the electron by the laser field (E_L) oscillating with a frequency (ω_L). In general the subscript L will refer to a parameter associated with the laser pulse. In a similar fashion to the previous diagnostic relations determined previously this parameter may also be written in a useful shorthand calculation form [2].

$$a_0 \simeq 0.84 \sqrt{I_0 [10^{18} \text{W cm}^{-2}] (\lambda_L [\mu\text{m}])^2} \quad (22)$$

The laser strength parameter allows another set of mathematical conditions to be noted, in the case where $a_0 < 1$ the electron quiver velocity is non-relativistic and the electric field influence on the electron motion dominates. When $a_0 \gg 1$ the quiver momentum becomes relativistic and as such a mass correction must be included and the figure of eight pattern of oscillation is seen (figure 1). Now a value that can determine the difference between the relativistic and non-relativistic case has been defined the equations and results found earlier must have a relativistic counterpart.

1.3.1 The Ponderomotive Force

One of the most interesting effects that arise once the nonlinear treatment is carried out with the plasma conservation of momentum equation (eq 8) is that of the ponderomotive force. This force presents itself as a drift in the electrons away from any electric field gradient. If the laser field has a constant spatial profile the electron will simply oscillate about its equilibrium position. If, however, the laser field has a spatially varying profile for example a Guassian envelope in space the electron will feel a differential drift velocity. Inspection of equation 23 describing the magnitude of the electron oscillation velocity shows that the velocity is directly proportional to the strength of the electric field. So if the electric field strength decreases as the electron moves the quiver velocity will also decrease.

$$|\mathbf{v}_{\text{osc}}| = \frac{eE}{m_e \omega_L} \quad (23)$$

This velocity variation across the pulse profile will manifest as a force that will act to push the electron away from the equilibrium position. This force is derived using an electric field solution of the form $E = E_0 \sin(\omega t)$ in equation 8 and using the second order velocity perturbations and their temporal derivative to determine a time average force component. This is the ponderomotive force and it is of the form;

$$F_p = -\frac{e^2}{4m\omega^2} \nabla \mathbf{E}^2 \quad (24)$$

It is this second order force that is the underlying mechanism that drives laser wakefield acceleration and this will be discussed in the next section.

1.4 Laser Wakefield

The laser wakefield accelerator was first proposed by Tajima and Dawson in 1979 [9] and operates based on the physical effects seen when a high intensity laser pulse propagates in a plasma. As seen in section 1.3.1 an intense laser pulse with a spatially and or temporally varying profile will cause a net force to act on the electrons in the plasma. This ponderomotive force will clear a large fraction of the electrons from the most intense region of the laser pulse and form what is known as the 'blow out' regime. The ponderomotive force may also be thought of as a radiation pressure acting to push on the electron fluid.

The displaced electrons attempt to return to their equilibrium position, the space charge now acts as a restoring force. This happens to the rear of the driving laser pulse once the action of the displacing force has been removed. The electrons then gather and form a high density wake and it is just ahead of this wake that electrons may be trapped and accelerated. The plasma acts like a transformer in that it converts the transverse electric field of the laser into an axial accelerating field by means of the ponderomotively formed wake.

This effect was imaged by A. Buck et al (2011) [19] in real time with a novel technique using Faraday rotation caused by the electron bunch itself. These observations show that this theoretical picture of the blow out region and accelerating wake are indeed correct.

1.4.1 Limits of Acceleration

Now that the mechanism of acceleration has been described what are the limiting factors to electron energy gain? A laser propagating in vacuum will undergo diffraction and the spot size will evolve as [1];

$$r_s = r_0 \left(1 + \frac{z^2}{Z_R^2} \right)^{\frac{1}{2}} \quad (25)$$

Where r_0 is the original spot size, z is the axial distance of propagation and $Z_R = \pi r_0^2 / \lambda_L$ is the Rayleigh length. Without some form of optical guiding, for example a plasma density channel or relativistic self-guiding, the laser will be limited to a few Rayleigh lengths.

The acceleration length will also be limited by the effects of electron dephasing, this is the scenario in which the accelerated electron outruns the accelerating wave. Consider a sinusoidal driving wave of the form $E_z = E_0 \sin[\omega_p(z/v_p - t)]$ this driving wave will have a phase velocity which is less than the speed of light in the plasma. An electron accelerated by such a wave will increase in velocity so that it approaches the speed of light. This means that eventually the electron will be moving with a higher velocity than the plasma wave and as a result will move into a decelerating region of the wave a lose energy. This process is known as dephasing and it will limit the acceleration length of a plasma based electron accelerator to a distance called the dephasing length L_d .

A highly relativistic electron in a linear plasma will have a dephasing length of;

$$L_d \simeq \gamma_p^2 \lambda_p \quad (26)$$

Where,

$$\gamma_p = \sqrt{1 - \frac{v_p}{c}} \quad (27)$$

is the Lorentz factor of the plasma (for further explanation of electron dephasing see [1] section II E). This means that the maximum energy gain after a dephasing length is given by the work done by the electric field in accelerating the particle (Tajima & Dawson 1979 [9]), assuming the linear regime $E_{max} < E_0$.

$$W_{max} \simeq eE_{max}L_d \quad (28)$$

In the Review of Modern Physics article by Esarey et al. [1] the electron acceleration is described as phase space orbits in momentum space (\mathbf{p}, ψ) . \mathbf{p} is the normalised electron momentum and $\psi = k_p \xi = k_p(z - v_p t)$. The electric field potential is then,

$$\phi = \phi_0 \cos \psi \quad (29)$$

The electron will be accelerated when it is in the phase region $-\pi < \psi < 0$. As the plasma wave is incident on the electron initially the phase velocity of the wave is greater than the velocity of the particle and the electron slips backwards through the wave. If the electron gains enough energy in the accelerating region of the potential then it will perform closed phase space orbits with the wave ($-\pi < \psi < \pi$), the electron is now trapped. If the electron does not gain sufficient energy then it will continue to slip back through the phase and out of the accelerating region.

A more complete version of the limiting conditions for electron dephasing, that includes the relativistic case also, is described in E. Esarey et al. (2004) [11] and is summarised in section III G of E. Esarey et al (2009) [1].

$$L_d \simeq \frac{\lambda_p^3}{2\lambda^2} \quad \text{for } a_0^2 \ll 1 \quad (30)$$

and relativistically,

$$L_d \simeq \frac{\lambda_p^3(\sqrt{2}/\pi)a_0}{2\lambda^2 N_p} \quad \text{for } a_0^2 \gg 1 \quad (31)$$

The term N_p represents the number of plasma periods behind the drive laser pulse.

The third major limiting factor of the acceleration length is pump depletion. This quite simply is due to the laser pulse using up its energy in driving the plasma wake. This effect was first predicted by Horton and Tajima (1986) [13] for a plasma beat wave accelerator. This length can be estimated as the distance over which the laser pulse will transfer all its energy to the plasma wake. In a similar fashion to the dephasing length the pump depletion length (L_{pd}) has been determined in the one dimensional limit in B. A. Shadwick et al. (2009) [12] and summarised in section III G of E. Esarey et al. (2009) [1] for the relativistic and non-relativistic cases.

$$L_{pd} \simeq \frac{2\lambda_p^3}{\lambda^2 a_0^2} \quad \text{for } a_0^2 \ll 1 \quad (32)$$

and relativistically,

$$L_{pd} \simeq \frac{2\lambda_p^3(\sqrt{2}/\pi)a_0}{\lambda^2} \quad \text{for } a_0^2 \gg 1 \quad (33)$$

The pump depletion length is the longest of the limiting factors so that the following inequality is satisfied [1];

$$Z_R \ll L_d \ll L_{pd} \quad (34)$$

The optimal laser wakefield accelerator will be limited only by the energy of the laser pulse.

1.5 Particle in Cell Code

In order to simulate the laser-plasma interactions a particle in cell (P.I.C.) code known as EPOCH was used. The vast number of particles involved and the number of variables that need to be recorded in even a small amount of material ($\sim 10^{23}$ for a few grams of Helium) mean that the simulation of any system will very quickly become extremely computationally expensive. The P.I.C. method represents large collections of particles as a smaller number of pseudo-particles. Figure 3 shows a flow chart to demonstrate the operation of the code, the first operation of the code before beginning this flow chart is to define a spatial grid on which to distribute the pseudo-particles.

This spatial grid must obey certain resolution conditions so that bulk motion may be observed as well as the smallest scales on which the plasma evolves. The principle condition which sets these resolution parameters is the plasma skin depth $\delta = c/\omega_p$.

$$D_{cell} \ll \frac{c}{\omega_p} \quad \text{or} \quad \lambda_L \quad (35)$$

$$D_{box} \gg \frac{c}{\omega_p} \quad (36)$$

The first condition, 35, ensures that the grid resolution is high enough to observe the plasma and its physical effects at the smallest distance scale over which it evolves. For an underdense plasma the laser wavelength is the shorter scale and so in the case of laser wakefield $D_{cell} \ll \lambda_L$ is the condition used. The second condition, 36, in simple terms sets the size of the simulation box so that it is large enough to capture the bulk motions of the plasma.

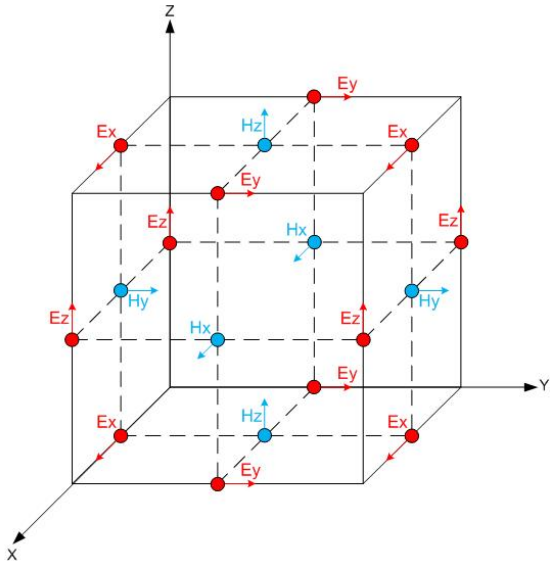


Figure 2: The Yee cell is a method of distributing the electric and magnetic field components onto a Cartesian grid [15]. The Lorentz force on each particle can then be determined using this field distribution

These conditions are very important in simulating the plasma wakefield because the small scale electron motion must be described so that the ponderomotive effects can form the wakefield and the box must be large enough to easily contain the wake and resulting plasma structures. The grid is defined so that it may represent the geometry of the surrounding medium, in this case vacuum. The grid also accounts for the dielectric properties and the permeability; both are their vacuum values here. Once the grid has been set the code will then distribute the particles onto the grid according to a defined density distribution ρ . Initially all the particles are stationary and so the current density is $\mathbf{J} = 0$. Once the particles are on the grid the fields associated with each particle are calculated using Maxwell's equations (11 - 14). These fields are then interpolated onto the grid so as to show the effect of each particle on all the others and the field effects of all the particles on each individual particle. Figure 2 depicts how the calculated magnetic and electric field components are represented with reference to a Cartesian coordinate grid.

The final part of the flow chart in fig. 3 describes the 'pusher'. This is the part of the code that actually moves of the particles using the Lorentz force equation to convert the fields into forces acting on the particles. The Lorentz force used in the P.I.C. code will have to be relativistic and so the equation in fig. 3 will have the form;

$$\frac{d\mathbf{p}}{dt} = q(\mathbf{E} + \mathbf{v} \times \mathbf{B}) \quad (37)$$

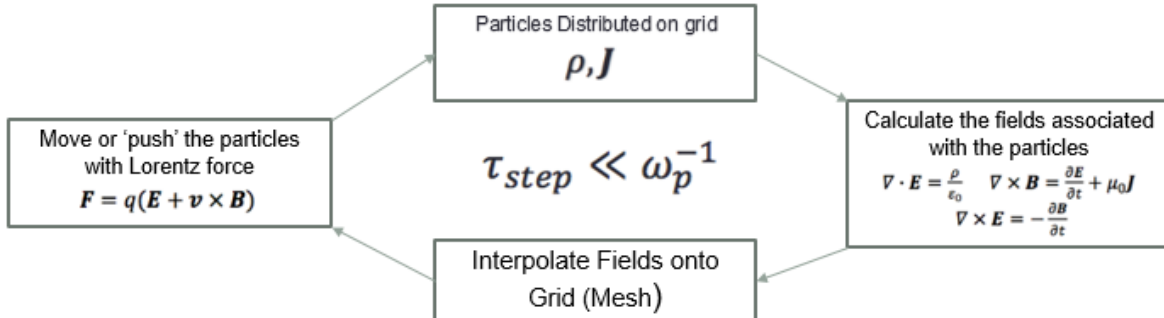


Figure 3: A flow chart showing the operation of particle in cell method.

Once the 'pusher' has moved all the particles a new density distribution is produced and this is fed back into the beginning of the cycle and the process begins again. The P.I.C. method considered here uses a finite difference time domain (FDTD) technique, this approximates the partial temporal derivative equations as a difference function (much like first principles derivatives) and calculates from one time domain to the next. This also means that a time step must be defined, in the center of the flowchart (fig. 3) there is the time step condition $\tau_{step} \ll \omega_p^{-1}$. This states that the time increment must be smaller than the inverse plasma frequency which is also equal to the plasma period. The condition means that the temporal resolution of the code must be shorter than the time scale on which the plasma evolves. For a more in depth mathematical explanation of the particle in cell method see a set of online notes compiled by R. Fitzpatrick [14].

1.5.1 EPOCH

The particle in cell code used to simulate plasma throughout this discussion is a second order relativistic P.I.C. code developed by the university of Warwick and is known as EPOCH. The code is based on the method outlined in section 1.5. The interface of EPOCH is straightforward as the user does not have to interact with the P.I.C. code directly but instead defines parameters and initial conditions using an 'input deck'. The users manual [10] details the complete set of inputs but here the most pertinent sections of input and code features will be outlined. The EPOCH code itself is split into three versions, each of which operates with a certain dimensionality, one dimension, two and finally a full three dimensional code. All of the results and simulations in this report were ran in the 2D EPOCH version.

The first block of the input contains the definition of any constants required examples can be seen in the appendix containing the input decks 6.1. After the constants are set the control block is inserted, this will be of the form;

```

begin:control
#number of grid points in domain
nx = 1500 #in x
ny = 300 #in y
#npart = 5 * nx * ny

# final time of simulation
t_end = 400 * femto

# size of domain
x_min = -30.0 * lambda0

```

```

x_max = -x_min
y_min = -15.0 * lambda0
y_max = -y_min
end:control

```

This control excerpt was taken from the pulse length variation section (2). The main function of the control deck is to define properties related to the simulation domain. Here 'nx' and 'ny' define the number of grid points in x and y respectively; the physical length of each of these dimensions is calculated using 'x_max' - 'x_min' and the same in terms of y. This section may also be used to enumerate the global number of particles in the box, however it is more useful for the simulations to put this in another deck as a density profile. The final function of this section is to give the final run time of the simulation. The full list of commands is available in the users manual [10].

Now that the computational and physical scales of the box have been defined the next question is what happens at the boundaries? This question is answered by the 'boundaries' block.

```

begin:boundaries
  bc_x_min = simple_laser
  bc_x_max = simple_outflow
  bc_y_min = periodic
  bc_y_max = periodic
end:boundaries

```

The conditions here are easily understood by considering the four walls of a box type domain where the minimum and maximum correspond to those set in the control deck above. There are a great many boundary conditions but only those used in the LWFA simulations are detailed here (see [10] for exhaustive list). The 'x_min' parameter is set as 'simple_laser' and this is because the driving pulse will be propagating from left to right and at the outset of the simulation the laser is set to be anchored to x_min. This condition allows EM waves to propagate with as little reflection as possible and particles are completely transmitted so this makes it the obvious choice for the boundary at which the EM pulse enters the box. At the opposite end of the region at 'x_max' the simple_outflow boundary is used and this has identical properties to simple_laser but it is 5% more computationally efficient [10]. Particles transmitted out of the domain at either of these boundaries will be removed from the simulation. Another condition with similar properties is the 'open' boundary which again transmits EM waves and particles without altering out-flowing characteristics removing them from the simulation. The final boundary set up to be discussed here is the 'periodic' type, an EM wave or particle incident on such a boundary is not removed from the simulation entirely but is removed at that boundary and re-emitted at the corresponding opposite. If one thinks of this event as the two opposite periodic edges actually forming a cylinder of continuous domain, as is the case for y edges in this particular simulation.

In order to populate the now spatially defined and boundary constrained simulation area the species block is inserted. This is where all of the various particle species required are set and regulated, this will be discussed generally here but the specifics of each set up will be covered in the methods section before each set of experimental results.

```

begin:species
  name = electron
  charge = -1.0
  mass = 1.0
  frac = 1.0
  temp = 0
  density = dens
  npart_per_cell = 5
end:species

```

Any species of particle is produced using it's mass and charge in electron masses and units of the elementary charge. The bulk properties are determined by a density value, a mass fraction (this is only used if the global number of particles is used in the control block. So this fraction will be the

percentage of the total number of particles taken up by this species.), a temperature and the number of computational particles per cell. The number of computational particles per cell must be sufficient to represent the density defined but not so high as to increase the simulation time considerably. A new species block must be included for each separate particle variety required this can be seen in the input deck section (6.1)

The box has been populated with electrons and ions. The ions are usually assumed to be stationary as they will no react on the electron time scale, this assumption can be included in a species block by including the flag 'immobile = T'. A laser pulse is now introduced to perturb the system and begin the laser wakefield process.

```
begin:laser
    boundary = x_min
    intensity_w_cm2 = 1.0e18
    lambda = lambda0
    profile = gauss(y,0,5*micron)
    #t_start = 0.0
    #t_end = 17.0 * femto
    t_profile = gauss(time,34*femto,17*femto)
end:laser
```

The variables in the laser input deck are fairly self explanatory and an in depth analysis can be found in the EPOCH users guide [10]. The time start and end lines, which are commented out, were used to form a square pulse. In the majority of set ups the Gaussian profile was used in time and space, the first variable in the parentheses is the dimension in which the Gaussian will act, second is on which value the profile is centred and the third is the full width half maximum (FWHM). So the code input $gauss(x, x_0, \omega)$ is a representation of the mathematical form [10];

$$f(x) = \exp\left(-\left(\frac{x - x_0}{\omega}\right)^2\right) \quad (38)$$

And in this expression the FWHM is given by

$$fwhm = 2\omega\sqrt{\ln 2} \quad (39)$$

There is a higher level of functionality in this deck including polarisation angle which can be used to adjust the direction of propagation and also focus a laser pulse. This focussing and the other features of the laser deck are considered in greater detail in the methods section of the focussing beam simulations (4.1).

Now that the mechanics of the code have been described, the domain computationally and physically set, the boundaries qualified and the box populated with particles the last component that remains is to detail the outputs of the code.

```
begin:output
    # number of timesteps between output dumps
    dt_snapshot = 10.0 * femto

    # Properties on grid
    grid = always
    ex = always
    ey = always
    ez = always
    bx = always
    by = always
    bz = always
    #jx = always
    #jy = always
```

```

#jz = always

#particle properties
particles = always + species
#px = always
#py = always
number_density = always + species
#mass_density = always
charge_density = always + species
#ekbar = always + species
temperature = never
end:output

```

A total run time of the system was stipulated in the control block, this total runtime is cut into output times with the command `dt_snapshot`. At each snapshot time the code will output properties, these properties are split into two categories. The properties associated with the grid, that is, the physical grid geometry and, as discussed in the P.I.C. code section (1.5) the fields linked to the grid by the Yee cell. The second category of output contains the properties of the particles, this includes momenta, number density, charge density, temperature etc. the users guide contains an exhaustive list [10]. The output of each of these properties is switched on and off using the terms 'never', do not output this data at snapshot, and 'always', do output at snapshot. If the simulation contains more than one species of particles the term '+ species' may be added in order to attach each quality to the particular species.

1.6 Testing the Code

Once the code had been compiled it was necessary to run simulations of known problems that would give results that could be easily compared to well understood theory and, or experiment. To test the Gaussian form and check the divergence of the magnetic field remained zero the simple case of a propagating Gaussian beam in vacuum was simulated. The term $\nabla \cdot \mathbf{B}$ will always remain zero and it is very difficult to cause it to be non-zero, the fields block, not discussed or used here, is the most probable way of altering the divergence of \mathbf{B} value. Line outs of the \mathbf{B} -field were taken using a Matlab code written for this purpose, in y (fig. 5) and also at different times during the pulse's propagation in x (fig. 4). The x line out (fig. 4) demonstrates that the magnetic field profile is constant as the pulse propagates.

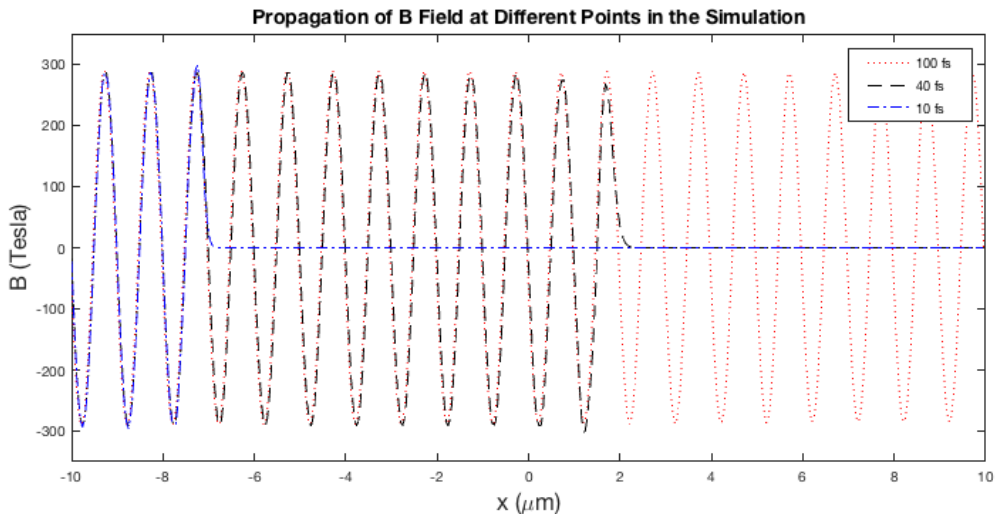


Figure 4: A set of overlaid line outs in the x direction, the direction of propagation, each taken at a different time in the simulation. The oscillatory profile is compatible with theory and expectation.

The next standard problem to be investigated with EPOCH was the two stream instability. This is a filamentation of electrons that occurs when two counter propagating beams of electrons encounter

one another. This instability occurs as a result of energy transfer between different electron velocity populations. The velocity distribution has a bump on the tail which is due to the injected electron stream in the plasma, without this population of fast moving electrons energy would not be transferred to the density wave (fig. 6). If the phase velocity is on the positive slope of this bump there will be a larger population of electrons moving faster than this wave and so energy will be transferred to the wave causing exponential growth. This manifests itself as the filamentation of the plasma into thin streams, the amplitude of these filaments will evolve as;

$$A = A_0 \exp\left(\frac{t}{\tau_{ch}}\right) \quad (40)$$

The inverse characteristic time is approximately equal to the plasma frequency which is determined by the number density of the electrons as seen in equation 16. This exponential amplitude growth describes how the number density of the filaments should increase and provides a useful diagnostic tool. The input deck was set up using the methods from section 1.5.1 and it can be seen in full in the appendix (6.1.1). Two electron species were introduced travelling in opposite directions with highly relativistic momentum $p = 2.7 \times 10^{-21} \text{ kg m s}^{-1}$ and a number density in the lab plasma range, $n_e = 1 \times 10^{18} \text{ cm}^{-3}$. The simulation was then ran for 500fs and snapshots taken every 5fs to monitor the growth of the density filaments.

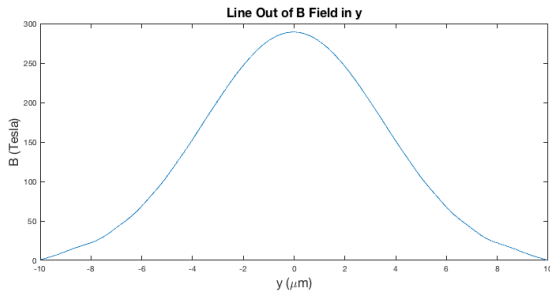


Figure 5: *A line out of the magnetic field along the y axis after propagating for 50fs. The analysis showed that the FWHM was consistent with the input parameters and expected behaviour.*

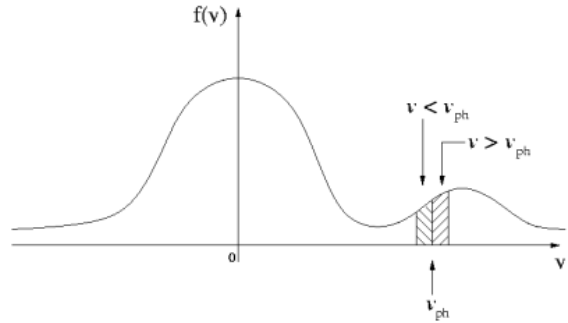


Figure 6: *In the two stream instability the electron velocity distribution has a distinctive 'bump' on the tail. Image source: Wikipedia, Author: Nherm commonswiki, https://commons.wikimedia.org/wiki/File:Bump_on_tail_dist.png*

To obtain the amplitude of the filaments, an analogue of the number density fluctuations in figure 7, a Matlab script was written that would take a line out along the y dimension at the midpoint of the x dimension (50 μm point in fig. 7). This cross-section had a sinusoidal profile and so a single parameter Fourier fit was performed and the amplitude found by the quadratic sum of the amplitude components. The amplitude, in terms of electron number density could then be plotted against time. Equation 40 was used to fit the data points and from this fit the plasma frequency could be determined and compared to theory in figure 8. The value of ω_p found using the code was,

$$\omega_p = 6.9 \times 10^{13} \text{ rad s}^{-1}$$

and this matched satisfactorily with the calculated value from 16,

$$\omega_p = 5.6 \times 10^{13} \text{ rad s}^{-1}$$

The agreement with theory was improved when the relativistic calculation was used $\Gamma = (\omega_p/\gamma_b^{3/8})\sqrt{\ln(\gamma_b^2)} \simeq 1.3\omega_p$, giving a relativistically corrected value of;

$$\omega_p = 7 \times 10^{13} \text{ rad s}^{-1}$$

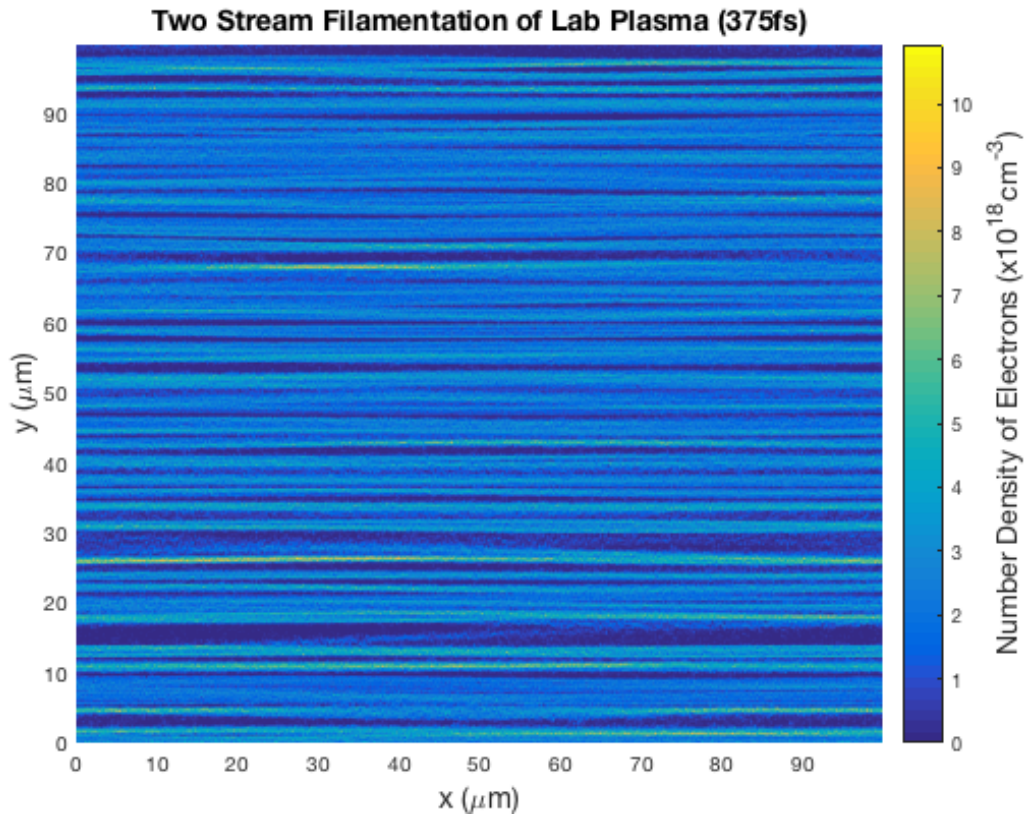


Figure 7: Filamentation of the electron beams is clearly visible here after 375fs. A density profile like this one could be produced for each 5fs interval.

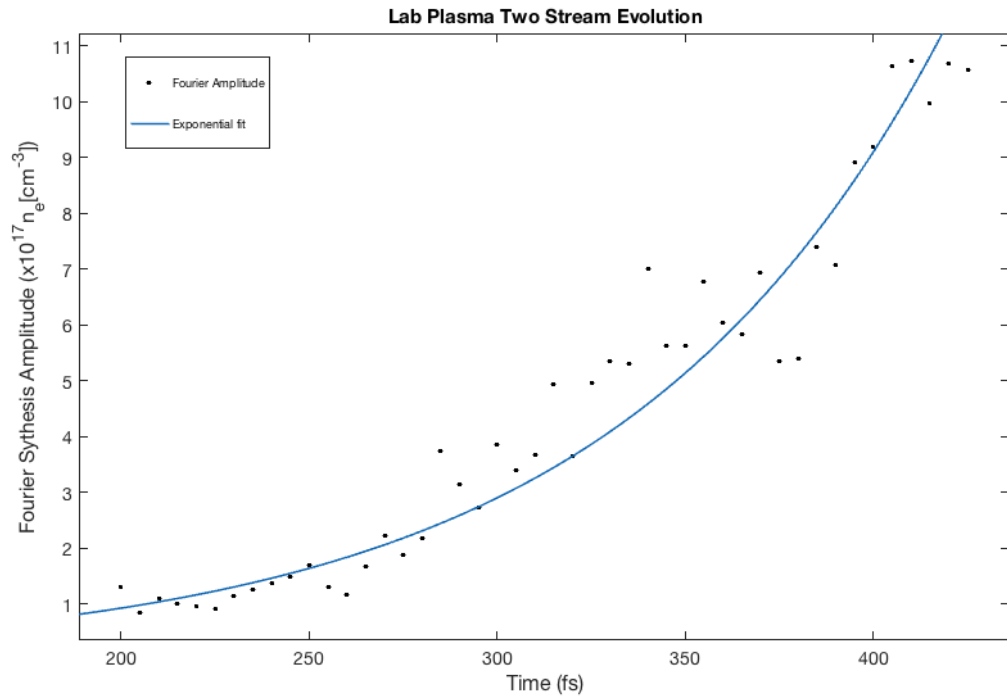


Figure 8: The Fourier amplitude calculated by the Matlab script at each time interval is shown as a black dot. The continuous line represents the exponential fit and this demonstrates that the amplitude does indeed increase as theoretically predicted.

2 Pulse Length Variation

The processes behind bubble formation and the electron motions that attempt to restore equilibrium causing a wake to form were outlined in 1.4. The parameters of the pulse and therefore how varying these parameters would alter the size of the blow out region were not considered. This section aims to investigate the effects of pulse length variation as well as the consequences of using different pulse profiles to drive laser wakefield.

The laser pulse was simulated in three separate regimes and these three lengths were applied to two different pulse shapes, firstly a Gaussian pulse and then a square wave form. The standard laser wakefield input deck was used to simulate these waveforms in epoch (see appendix 6.1.2), all values were held constant except those altered to change the pulse length or shape, a fully ionised cold Helium plasma was used for the following simulations. The constant values were intensity $I = 1 \times 10^{18} \text{ W cm}^{-2}$, the total time of simulation (unless stated) $\tau_{total} = 400\text{fs}$, the time between snapshots $\tau_{snapshot} = 10\text{fs}$, the plasma electron density $n_e = 1 \times 10^{18} \text{ cm}^{-3}$, the ion density $n_{ion} = 0.5 \times 10^{18} \text{ cm}^{-3}$ and the laser wavelength $\lambda_0 = 1\mu\text{m}$.

The plasma frequency was calculated from the equation,

$$\omega_p = 5.64 \times 10^4 \sqrt{n_e [\text{cm}^{-3}]}$$

and this gave a value of $\omega_p = 5.64 \times 10^{13} \text{ rad s}^{-1}$. From this the plasma wavelength could be calculated using the relation,

$$\lambda_p \simeq \frac{c}{\omega_p} = 5.31 \mu\text{m}$$

this plasma wavelength was used as the test condition for the pulse length. Three pulse lengths (L) would be tested so that the following conditions were met, the pulse was assumed to travel at the speed of light so the length of the pulse in time could be determined.

$$L < \lambda_p, \quad L = 0.6 \mu\text{m}, \quad \tau_{pulse} = 2\text{fs}$$

$$L = \lambda_p, \quad L = 5.3 \mu\text{m}, \quad \tau_{pulse} = 17\text{fs}$$

$$L > \lambda_p, \quad L = 30 \mu\text{m}, \quad \tau_{pulse} = 100\text{fs}$$

The results of each pulse length and profile are shown hereafter in the form of number density plots and line outs of the electric field profile.

2.1 Methods

The input deck was written and is shown in section 6.1.2, the laser parameters specified in the introduction above were held constant and only the pulse profile and length were altered. The domain was a 1500x300 grid with a spatial extent of $60\mu\text{m} \times 30\mu\text{m}$. The laser pulse would very quickly propagate out of this box and not show how the plasma evolved over a longer scale. So that it was not necessary to simulate a long and computationally expensive capillary of plasma a moving window feature was used.

```
begin:window
  move_window = T
  window_v_x = c_l
  #when pulse is centered in window
  window_start_time = (x_max - x_min)/c_l
  bc_x_min_after_move = simple_outflow
  bc_x_max_after_move = simple_outflow
end:window
```

This input block enables the defined domain to move with a certain velocity and so track the physical interaction of the laser and plasma. The block sets a movement speed, the speed of light, and a time at

which to move. The start time was determined by a speed-distance-time calculation that initiated the boxes movement when the laser pulse had reached the center of the domain. The last two statements reassign the boundary conditions once the movement has begun (boundary conditions are discussed in 1.5.1).

The square pulse was achieved by starting the laser at a particular time ($t = 0$) and then cutting it off again once the desired pulse length had been reached. The three pulse length conditions were then simulated and the results analysed by the Matlab scripts written for this purpose. The two scripts most used were the NumberDensityProfile and LineOut. The density profile program's main purpose was to read in the total number density from the sdf file (the file type output by EPOCH) along with the simulation grid before plotting both as a 3D surface image. The relative heights of the 3D surface overlaid onto the simulation grid represented the number density of electrons. In order to present this plot in a more easily interpreted manner the plot was viewed top down, looking down on the 3D surface. Now the density peaks could be represented using a smooth colour contour variation which is quantified using a colour bar set with the plots. The line out script was simply an extension of the number density program as it took as line along one dimension and plotted the number density or electric field along the desired line.

The Gaussian pulse was possible using a built in Gauss function in the code and this is explained in 1.5.1. Again, the three pulse lengths were simulated and the results analysed in the same manner.

2.2 Results

2.2.1 Square Pulse

Figure 11 shows the line out taken from the Epoch data. The trailing edge does have a shallower electric field gradient due to the code, however, the leading edge shows a strong sharp square pulse gradient.

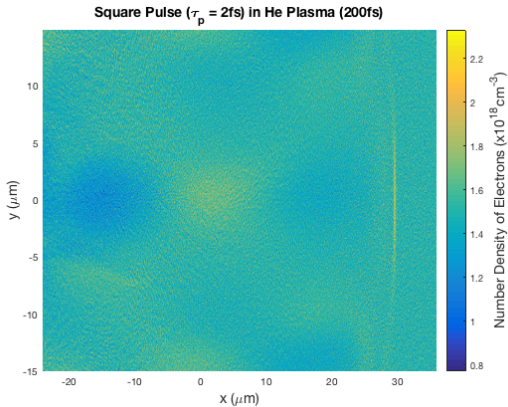


Figure 9: The 2fs square pulse does not form a low density region. The short pulse length will correspond to a short exposure time for the electrons to the ponderomotive force. The electrons effectively will not experience enough of a push to displace them sufficiently for wake formation.

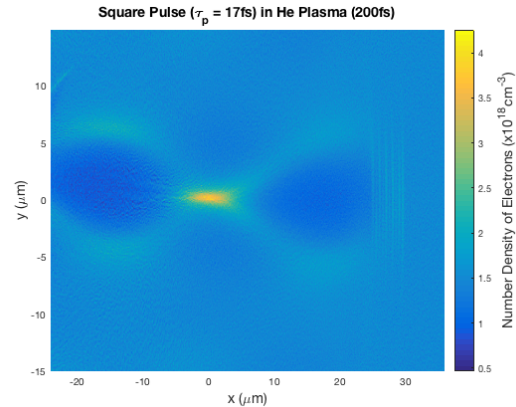


Figure 10: The 17fs square pulse forms a better bubble as the ponderomotive force is proportional to the gradient of the electric field and the square pulse has a very steep gradient compared to the Gaussian.

The square pulses in all three regimes show a more pronounced blow out of the bubble than is observed in the Gaussian pulse (2.2.2), this is because the ponderomotive force (equation 24) is proportional to the electric field gradient which is much greater at the leading edge of the square pulse.

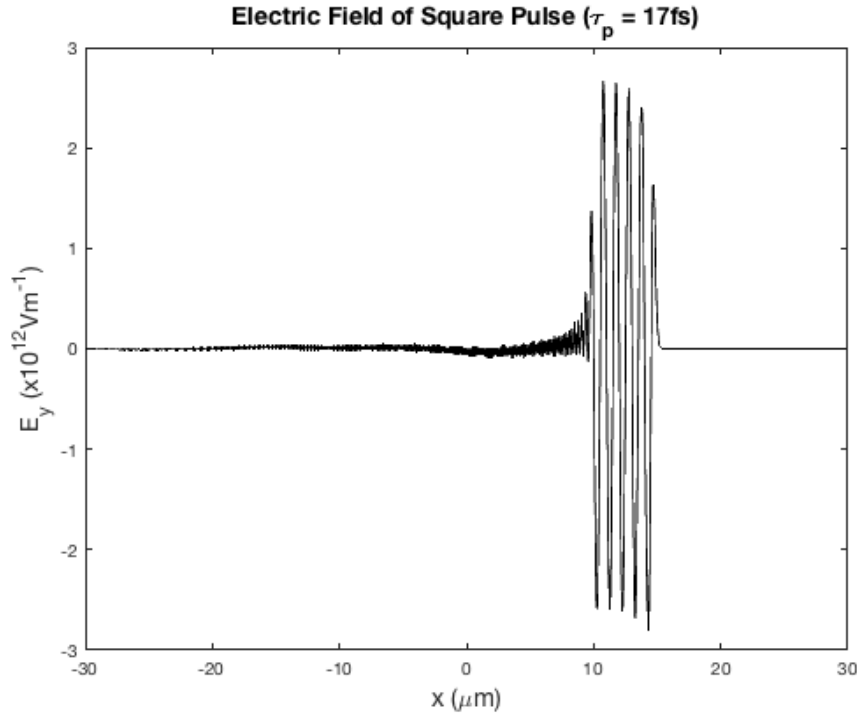


Figure 11: A line out of the square profile waveform. The sharp cutoffs leave numerical artifacts at the trailing edge of the pulse, these can be seen as the erratic but small field variations in the wake of the pulse. This line out was taken after 150fs to produce an illustrative plot of the pulse profile.

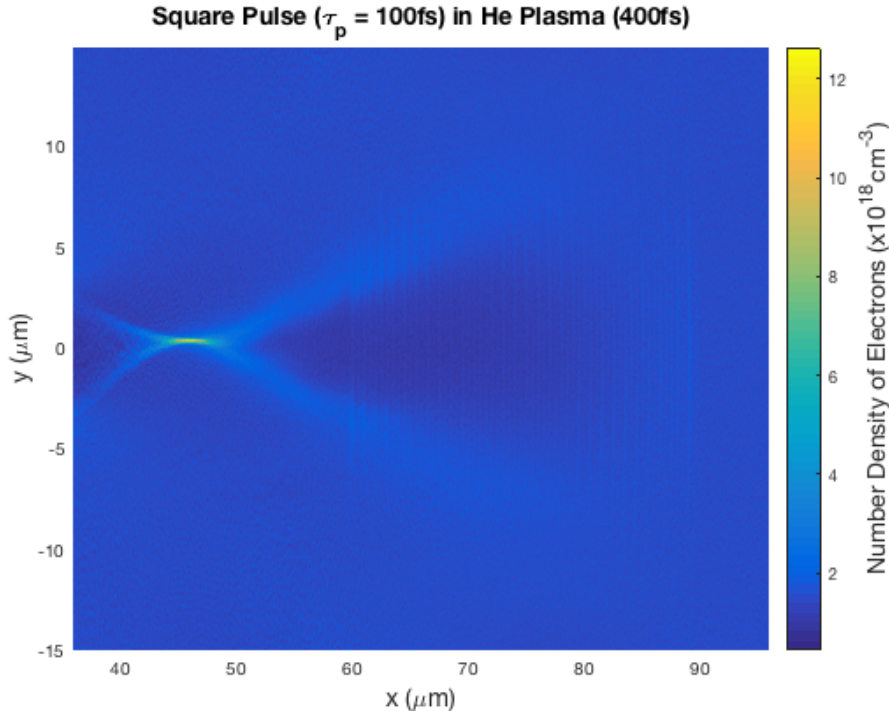


Figure 12: The 100fs square pulse forms the blow out regime more quickly than the Gaussian pulse, the low density bubble is also much broader.

The square waveform demonstrates that the $L = \lambda_p$ (fig. 10) condition forms the low density bubble region and this also is able to propagate much further than the other conditions. The short pulse does not cause blow out and the much longer 100fs pulse is unstable. These instabilities are caused by the length of the pulse, as the ponderomotive force pushes the electrons out of equilibrium at the leading edge of the laser the induced space charge recalls the electrons to equilibrium. In the case of the short pulse this initial push is not felt for long enough to reduce the electron density effectively (fig. 9). Conversely the $\tau_p = 100\text{fs}$ pulse pushes the electrons for too long and prevents the wake being formed properly (fig. 12). The $L = \lambda_p$ condition on the other hand is stable because the leading edge push is long enough to displace the electrons but not so long that the number density peak at the back of the bubble is prevented from forming. The situation is further improved as the electrons feel a second push from the gradient at the rear of the pulse when the $L = \lambda_p$ condition is met.

2.2.2 Gaussian Pulse

The Gaussian pulses were introduced to the plasma with the same conditions as the square pulse so the two different wave forms could be compared under similar conditions. From a code perspective the Gaussian form (fig. 15) does not show the numerical instabilities that the square form did in its wake. This is most likely due to the smooth variation of the electric field amplitude across the Gaussian envelope in contrast to the abrupt cut off required for the square. With the resolution conditions of the spatial grid (1.5) in mind these instabilities may be explained. The grid resolution is set such that $D_{cell} \ll \lambda_L$ and this allows the variation in the oscillating electric field profile to be observed. The sharp cut off of the electric field likely violates this condition and hence numerical instabilities are introduced.

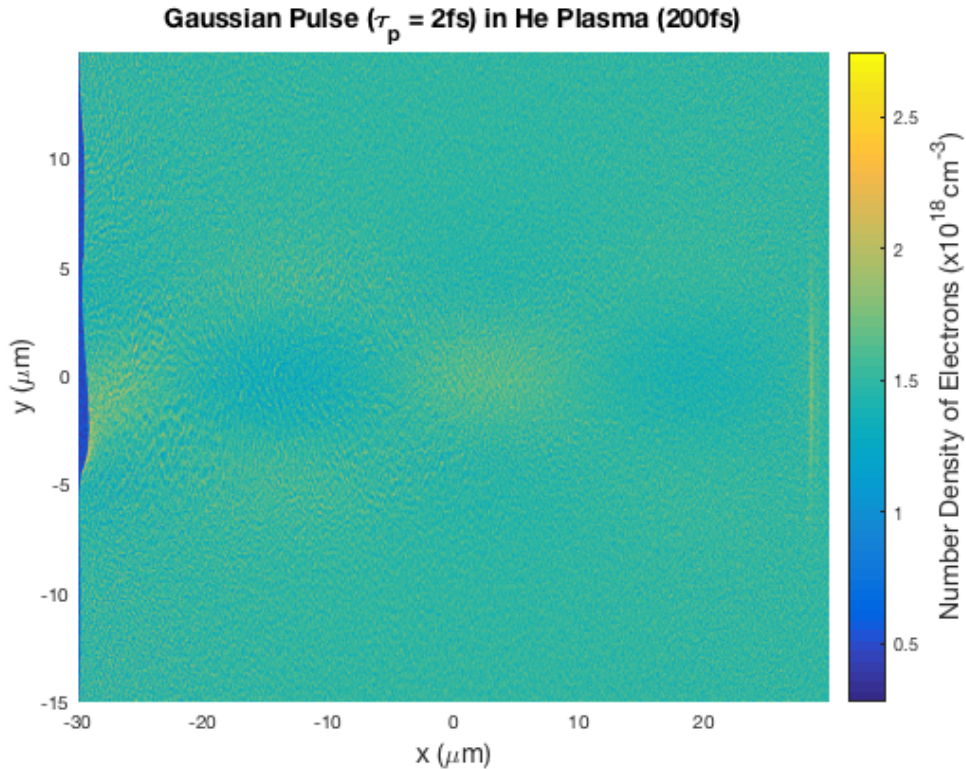


Figure 13: The result from the Gaussian pulse with a characteristic width of 2fs. This snapshot shows the plasma electron density variation after 200fs. The short laser pulse has not produced the low density bubble associated with laser wakefield acceleration, there is a slight density variation however this is not enough to produce accelerated electrons.

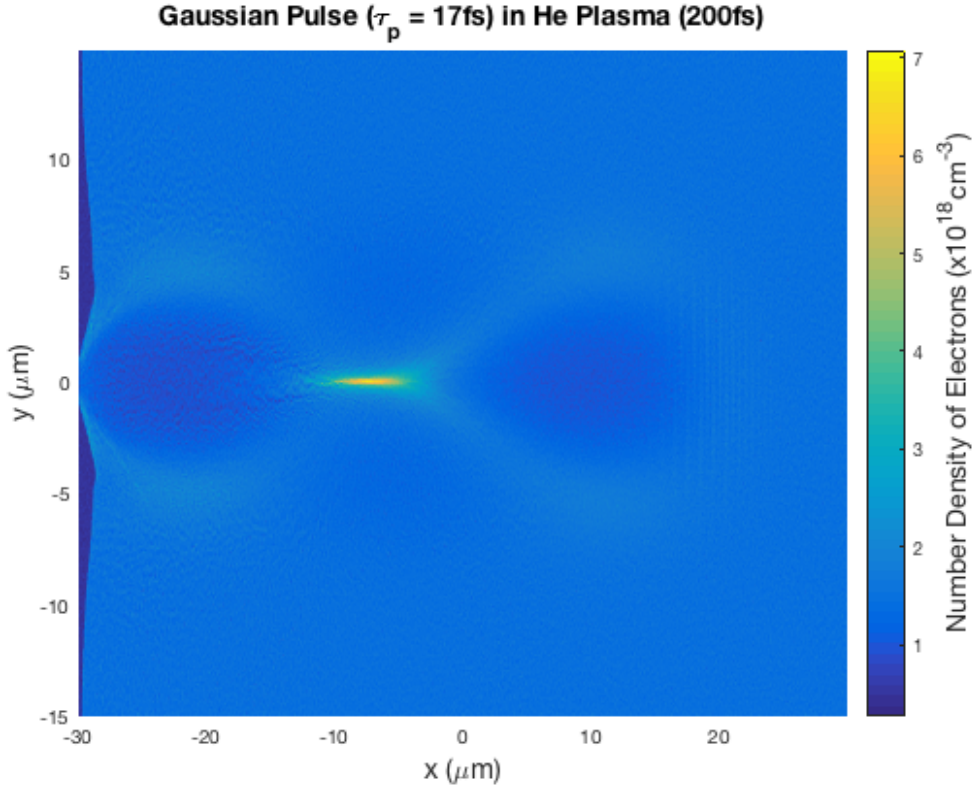


Figure 14: The pulse length in this figure is equal to the plasma wavelength and this is the optimised situation for laser wakefield acceleration. The low density bubble is clearly visible and it propagates for the duration of the simulation.

A lineout of the Gaussian waveform used to produce the density profile in figure 14 is shown in figure 15. The pulse length in each of these cases describes the characteristic width of the Gaussian distribution, ω . The full width half maximum is calculated using equation 39 and a full description of the Gauss function is given in section 1.5.1.

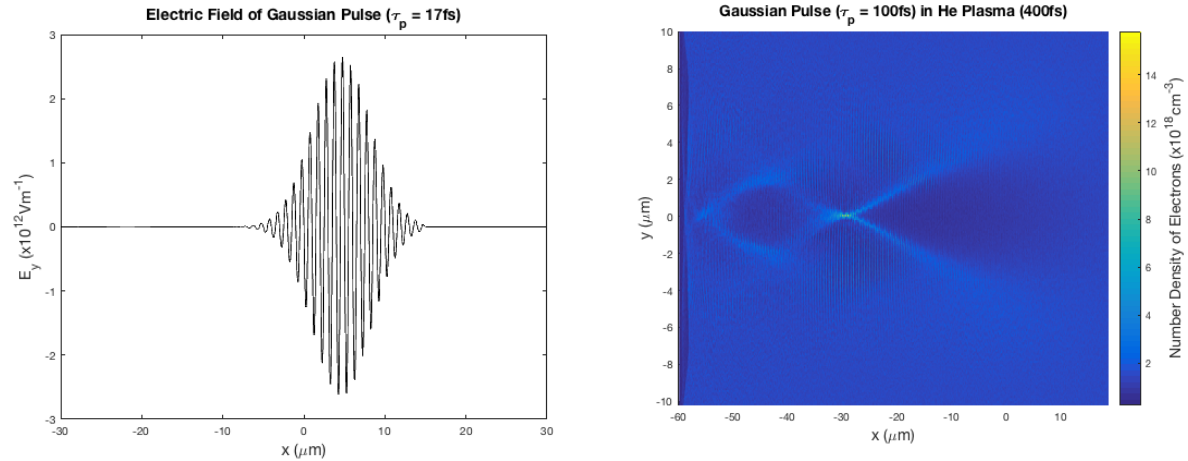


Figure 15: A line out of the Gaussian profile in y . This lineout was taken after 150fs, this time was chosen purely for demonstration purposes to show the form of the pulse.

Figure 16: When the pulse length was set to be much longer than the plasma wavelength the low density region caused by the ponderomotive force is formed, however, the region is large and unstable. The blowout regime took longer to form and this plot show the simulation after 400fs which is twice as long as the optimised $L_{pulse} = \lambda_p$.

Figure 16 shows the features of instability in the bubble region. Ahead of the wake there appear two streamer type structures and these are a sign of instability. The Gaussian enveloped laser demonstrated the same result obtained using the square pulse in that the $L_{pulse} = \lambda_p$ case is optimal for wakefield production. The Gaussian pulse also produced a higher amplitude plasma density wave without any of the numerical instabilities and this is shown in the next set of data.

2.2.3 Electric Field for $L = \lambda_p$

The form of the accelerating electric field caused by wakefield formation is demonstrated by lineouts of the electric field in the idealised $L = \lambda_p$ condition.

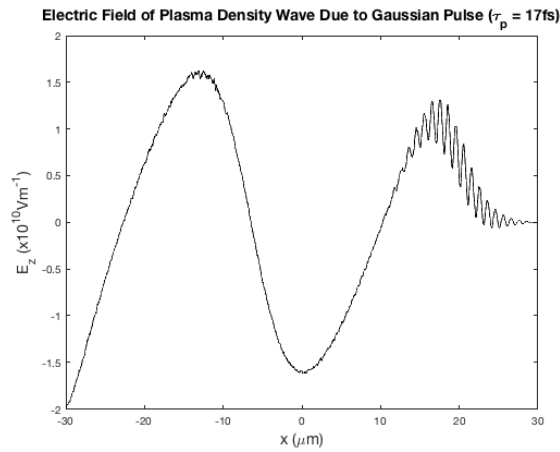


Figure 17: The Electric field due to the electrons displaced by the driving laser pulse. The effect of the laser pulse can be seen at the leading edge of the wakefield, the pulse is travelling left to right. Behind this is the electric field caused by the increased electron density.

The 17fs Gaussian laser pulse had a max amplitude of;

$$E_{max} = 1.6 \times 10^{10} \text{ V m}^{-1}$$

for positive and negative peaks.

The maximum amplitude for the negative electric field of the square form in fig. 18 directly behind the pulse is similar to the Gaussian but marginally larger.

$$E_{max} = -1.618 \times 10^{10} \text{ V m}^{-1}$$

The positive peak of the E-field is larger than the Gaussian

$$E_{max} = 1.863 \times 10^{10} \text{ V m}^{-1}$$

The theoretical maximum electric field strength for this density given by equation 20 is $E_0(max) = 9.6 \times 10^{10} \text{ V m}^{-1}$. This is considerably stronger than the fields induced here.

The purely electric field line outs of figures 17 & 18 can be compared to the density profiles along the same line. These comparative plots (figs. 19 & 20) show the large amplitude density peak of the wake and the accelerating field. The red lines in figure 19 show the region of acceleration, this region is just ahead of the negative maximum of the electric field up to the point that the electrons begin interacting with the magnetic field of the pulse. The electrons can be seen under the influence of the field by the higher frequency oscillations at the right hand edge of the electric field profile in both figure 20 and figure 19.

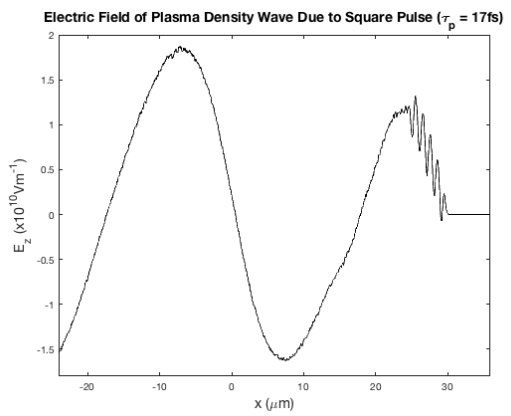


Figure 18: This line out depicts the Electric field due to the electrons and the driving square laser pulse, in comparison to the Gaussian the form is similar excluding the difference in the laser pulse at the leading edge.

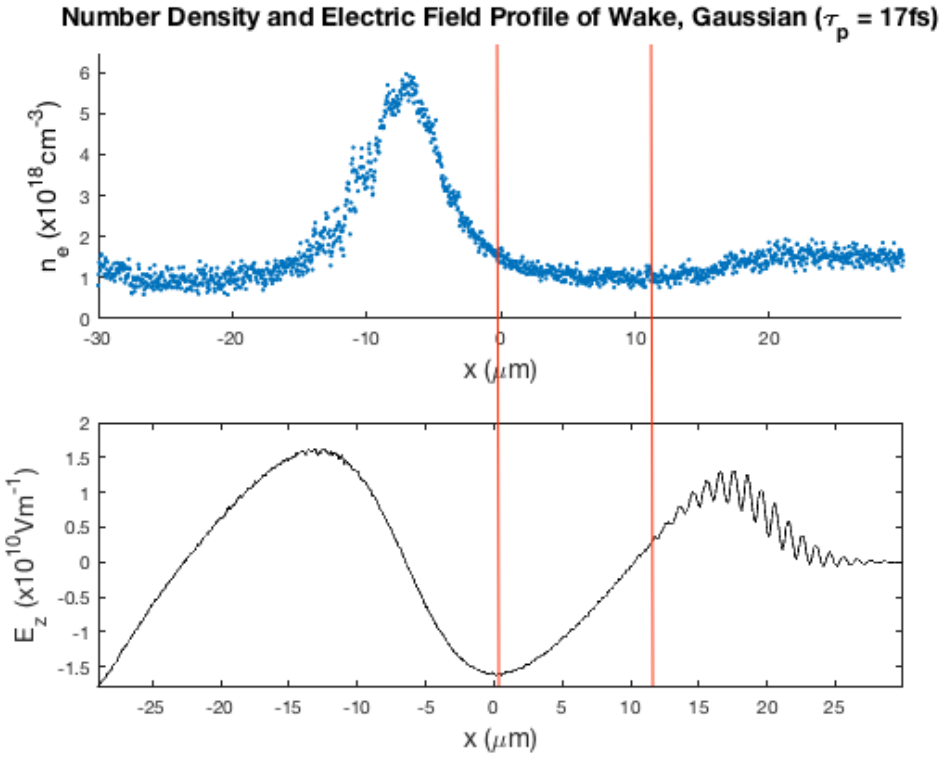


Figure 19: A comparison between the number density profile and the electric field of the wake for the Gaussian pulse. The density profile shows that an empty bubble region has formed. The red lines indicate the acceleration region where electron trapping will take place.

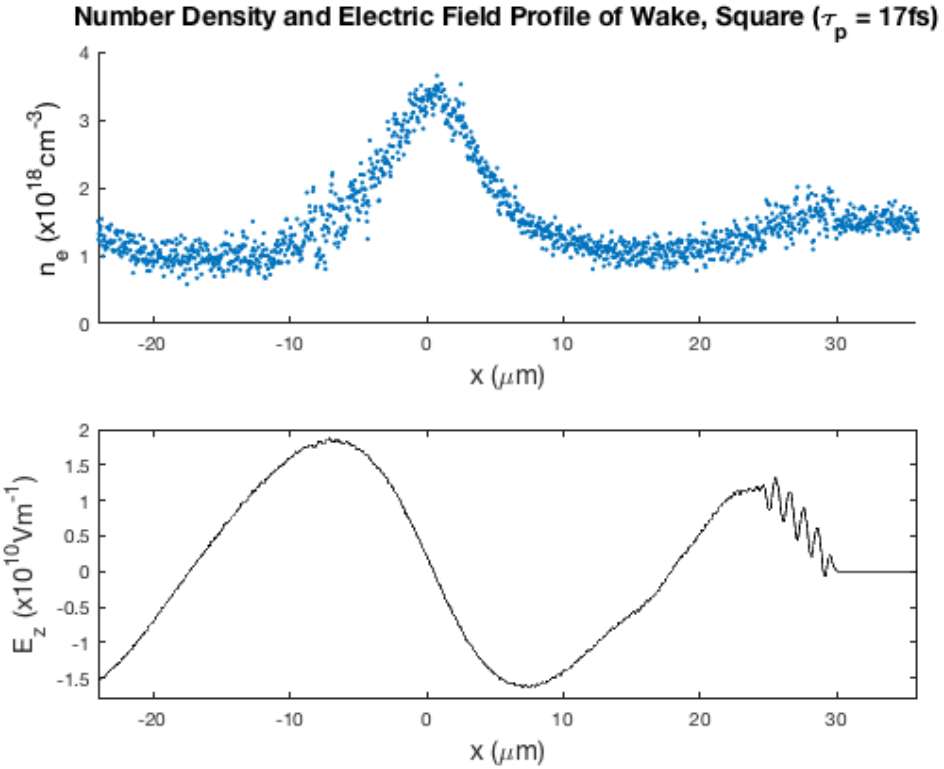


Figure 20: A similar number density to electric field profile comparison but for a square pulse. The peak number density in this case is less than that achieved using the Gaussian pulse in fig 19.

The higher frequency oscillations in the number density profile and induced electric field are due to the magnetic field interaction with the electrons. When the intensity of the laser is large enough to mean that the magnetic field component is comparable to the electric the electron will feel a force in the propagation direction of the EM wave (see section on Non-Linear effects, 1.3). The effect of this periodic movement is what is being observed in these plots and as such will oscillate with twice the laser frequency, $2\omega_L$.

2.3 Discussion

As considered in the introduction the wakefield should be most efficiently driven when the pulse length is of the order of the plasma wavelength. The results here clearly show this to be true as the most stable and long lasting bubble formation occurred when $L = \lambda_p$. This conclusion could be further confirmed by simulating a range of pulse lengths between the $L < \lambda_p$ and $L > \lambda_p$ limits. The number density and field comparison plots show that the Gaussian pulse forms a very well defined blow out region (fig. 19). This well formed bubble and the fact that the square pulse introduces numerical artefacts in the wake of the pulse means that the Gaussian pulse with the condition $L \sim \lambda_{plasma}$ will be the standard pulse type in the rest of the investigations.

3 Injection Methods, Nitrogen Trapping

Section 2 demonstrated the changes observed in the bubble formation and wake propagation due to pulse length variation but in each of the cases there were no injected electrons. This section will investigate how the introduction of Nitrogen neutrals changed the number density of electrons in the accelerating region of the plasma wave. The method of injection considered here is the tunnel ionisation of tightly bound electrons in the inner shells of higher atomic number neutrals (higher Z relative to Helium). This method is excellently treated in A. Pak et al. (2010) [17] and forms the basis of this investigation.

In section 2 the plasma was preformed, meaning that the electrons were already dissociated from the Helium nuclei. The input deck was set such that the Helium nuclei had a fixed, smooth and continuous density profile that did not change during the simulation as the heavy nuclei were considered to be stationary over the electron-laser interaction time scales. The electron fluid was then overlaid with a smooth and continuous density profile that corresponded to the scenario in which all the electrons of every atom had been ionised. A laser pulse was allowed to propagate and the effects thereafter observed. These set up conditions would not allow for ionisation injection methods to be used so the input was modified to make use of EPOCH's built in ionisation regimes.

The control block (1.5.1) allows for three different ionisation processes and each can be enabled by using the 'T' flag (e.g. field_ionisation = T). The first of the ionisation processes is that of multiphoton, in simple terms this is the physical process by which ionisation may occur with photons that by themselves do not have sufficient energy to ionise an electron. If the intensity is high enough the electron may absorb a photon and move to an extremely short lived virtual state (not a stable energy level) and before it decays absorb another photon and so in a series of steps reach the required energy for complete ionisation. An article by C. Mainfray and C. Manus (1991) [18] gives a detailed consideration of multiphoton ionisation.

This type of process can occur by two slightly different paths, the first is that the photons raise the electron through a series of virtual states to the ionisation energy and the second is that one of the states in the series of steps is real as in figure 21. The latter process is considerably more likely and the reason for this becomes clear when one thinks of the relative lifetimes of real and virtual atomic states. The real states are much longer lived than the virtual and so if the electron is promoted to one of these real states it can spend much longer waiting to absorb more photons and hence dissociate.

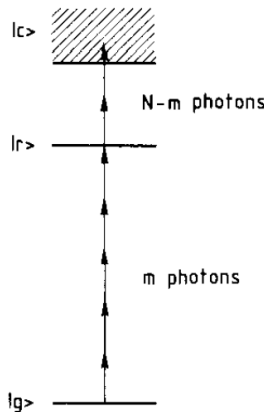


Figure 21: This figure taken from C. Mainfray & C. Manus (1991) [18] shows pictorially the multiphoton ionisation process. The small arrows represent the photons promoting the electron to the virtual states. The solid line Ir shows the real atomic energy level so this is the resonant case.

The next two ionisation regimes are linked and also the principle mechanism on which the tunnel ionisation injection is based. The Coulomb potential well in which the electrons sit is deformed in the

presence of an electric field, like that of an intense laser pulse. If the electric field is strong enough the barrier may be deformed, and completely suppressed, so that the electron has a 100% chance of ionisation without requiring any energy. Analogous to this, figure 22 demonstrates the result of an electric field not being strong enough to suppress the potential well entirely. In this setting a portion of the barrier potential remains so that an electron would have to tunnel quantum mechanically free and this is a probabilistic process.

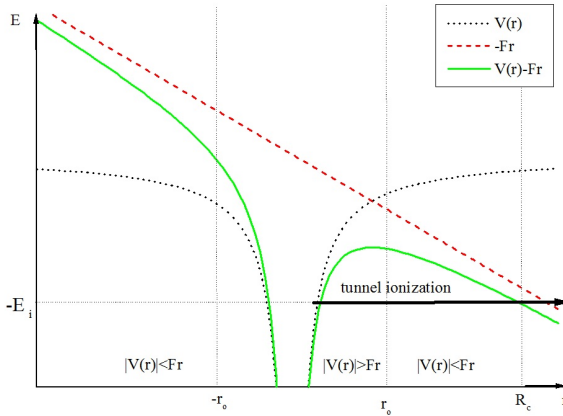


Figure 22: *Tunnel ionisation occurs when the electric field of a laser, for example, deforms the Coulomb barrier to the point that quantum mechanical tunnelling of the electron may occur. The red dashed line shows the deforming electric field, the black dotted line is the original potential well and the solid green line represents the combined effect of the two. One can now see the barrier seen by the electron has a finite tunnelling probability.* Image source: Wikicommons, Author: Abdossamad Talebpour

The principle behind this injection method is that along a Gaussian pulse profile the strength of the electric field oscillates as it should but also grows in amplitude according to the envelope. This means that the electrons with lower ionisation energies will be barrier suppression ionised at the front of the pulse and hence experience the ponderomotive force for the duration of the pulse and form the wakefield structure (see 1.4). Both of the Helium electrons and the five outer Nitrogen electrons will be ionised in this way. The two inner K shell electrons which are tightly bound ($I_p = 553.97\text{eV}$ & 669.34eV [20]) will only have the barrier deformed enough for tunnel ionisation at the peak of the Gaussian pulse. Electrons that tunnel free and are ionised here will appear in the accelerating region of the wave. These electrons will be liberated and appear stationary to the plasma density wave and if they can gain enough energy that they move with the plasma density wave they will become trapped and be further accelerated.

3.1 Methods

The EPOCH input deck set up was similar to the pulse length variation investigation but with several additions and modifications. The plasma was not preformed and the domain was populated with neutral atoms which needed to be ionised by the laser pulse. The ionisation processes outlined in 3 were enabled in the control deck and a modified species block for Helium and Nitrogen neutrals added.

```
begin:species
#He
name = Helium
charge = 0.0
mass = 4.0 * 1830
npart_per_cell = 4
immobile = T
ionisation_energies = (24.6*ev,54.4*ev)
ionisation_electron_species =
```

```
(He_electron,He_electron)
density = 0.5e25
temp = 0.0
end:species
```

The Helium neutrals, like the ions used before were immobile. The mass of the species was required as before as was the charge but the charge was zero as the atoms were neutral. The ionisation energies were entered into a list and the 'ionisation_electron_species' command allowed a complimentary list of electron names to be defined. EPOCH would naturally assign an electron species name and an ordinal number to the ionised electrons, 'Helium1' and 'Helium2' for example. The general species name in 'ionisation_electron_species' was also added so that the total electron contribution from a species could be easily plotted. The Nitrogen neutrals were similarly defined and the full input deck can be seen in [6.1.3](#).

The laser parameters were as follows

$$I_0 = 8 \times 10^{18} \text{ W cm}^{-2}$$

$$\tau_p = 18\text{fs}$$

$$\lambda = 0.8\mu\text{m}$$

and these remained constant throughout the investigation. The effect of different concentrations of Nitrogen relative to the Helium number density were of interest in these simulations. The parameter that was altered then was the number density of nitrogen neutrals from 0% to 10% (these percentages are given as a percentage of the Helium number density).

The results from the simulations were analysed using the density profile Matlab script and another code that was written to output an energy spectrum of the electrons. The code read out the momentum matrices in x and y for every particle and then determined the electron energy by using the particle momenta to solve the relativistic energy equation;

$$E^2 = p^2 c^2 + m_0^2 c^4 \quad (41)$$

Once this energy matrix had been determined a histogram was plotted to show the number of particles with each energy and so give an energy spectrum for the electron population.

3.2 Results

3.2.1 0% - 10% Nitrogen ($n_{He} = 5 \times 10^{18} \text{ cm}^{-3}$)

The pulse was allowed to propagate in a neutral Helium gas with number density of $n_{He} = 5 \times 10^{18} \text{ cm}^{-3}$. The neutral He was fully ionised by the pulse via barrier suppression ionisation [\(3\)](#). Figure [23](#) shows the point at which the outer electron was ionised (just to the left of 1020μm), the ionisation points can be seen where the number density is increasing by steps just ahead of the pulse. The vast majority of the electrons ionised in this way form the wakefield structure and only a very small fraction are actually trapped and accelerated. The density profile and electric field line outs in figure [24](#) demonstrate that an empty bubble region is formed. If a significant number of electrons were trapped there would be another density spike just ahead of the negative maximum of the electric field (see figure [19](#)). The energy spectrum produced for the pure Helium system also demonstrates that the low energy wake forming electrons are present with only a few electrons at slightly higher energies, figure [30](#).

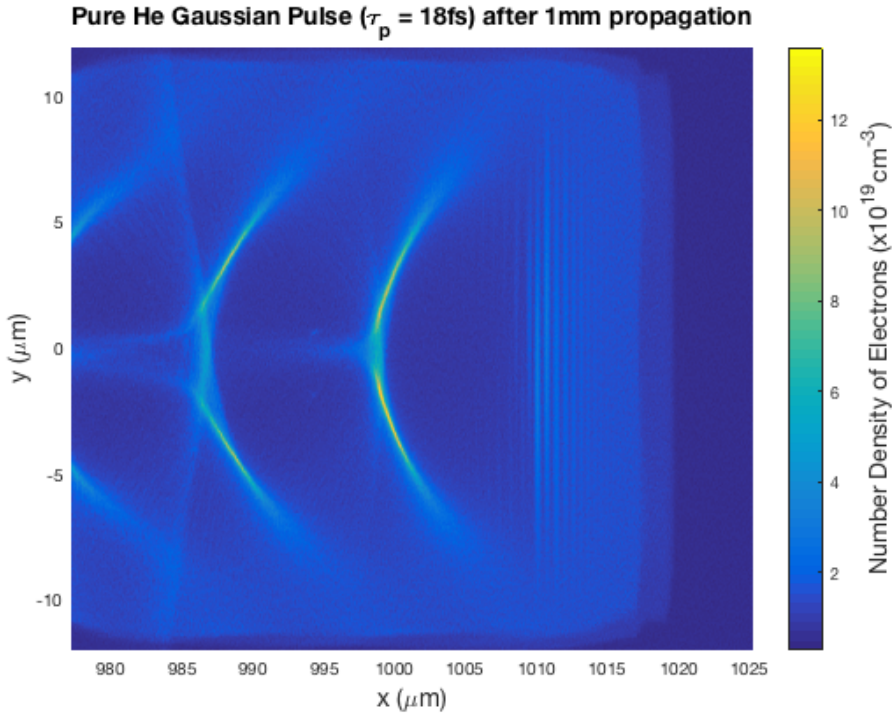


Figure 23: Using the Gaussian enveloped pulse with parameters described in 3.1 the following electron number density plot was produced. The pulse was allowed to travel through neutral Helium ($n_{He} = 5 \times 10^{18} \text{ cm}^{-3}$)

One notices a train of wakes in fig. 23 rather than the single blow out regime and wake shown in the pulse length variation section (2). This is a consequence of the original perturbation by the ponderomotive force, although the pulse has passed and there is no driving force the electrons continue to oscillate about their equilibrium position. The space charge induced by the low electron density region (leaving only the positive nuclei) calls the electrons back but they overshoot and the effect repeats with a decaying amplitude. This is very similar to a classical damped harmonic oscillator.

As described in the methods section (3.1) Nitrogen neutrals were introduced so that inner shell electrons were tunnel ionised in the accelerating region and these electrons appearing stationary to the wake have a larger probability of becoming injected. Figure 25 is an electron number density plot of the system after the pulse has been allowed to travel for 1mm. A noticeable bunch of electrons is seen in the blow out region just ahead of the wake, these electrons have gained enough energy to be trapped and are propagating along with the pulse. The length over which the electrons will remain in the bunch and continue to gain energy will be limited by the factors discussed in 1.4.1.

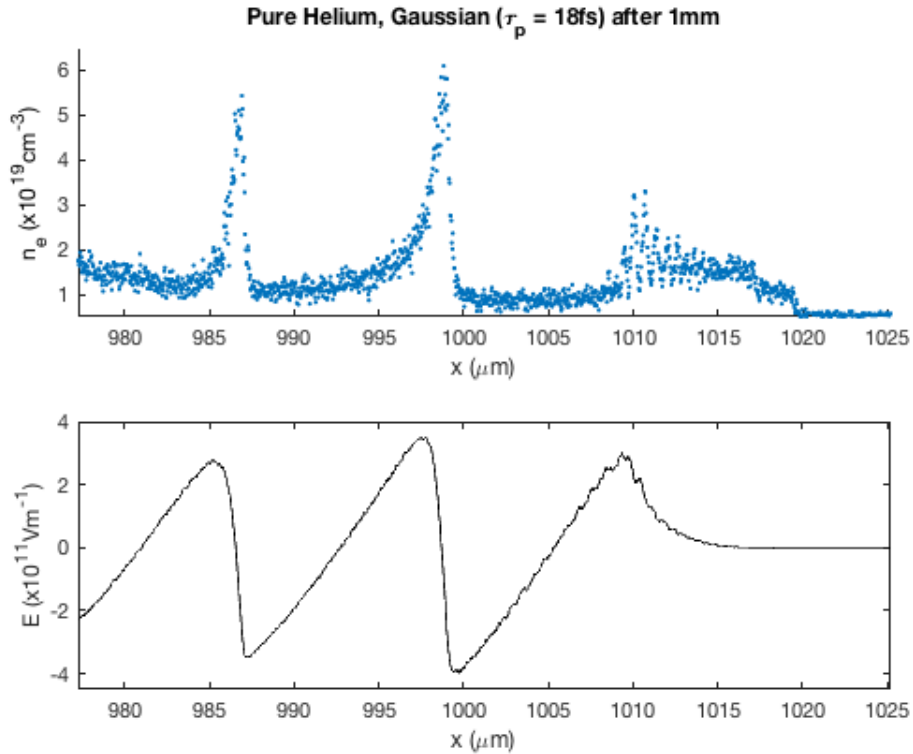


Figure 24: A comparison of the density profile to the electric field line out. This plot is informative in that it demonstrates the relation between electron density perturbations and the electric field caused by the large amplitude plasma wake. This large electric field is what is used to accelerate the electrons that are able to gain enough energy and move with the density perturbation.

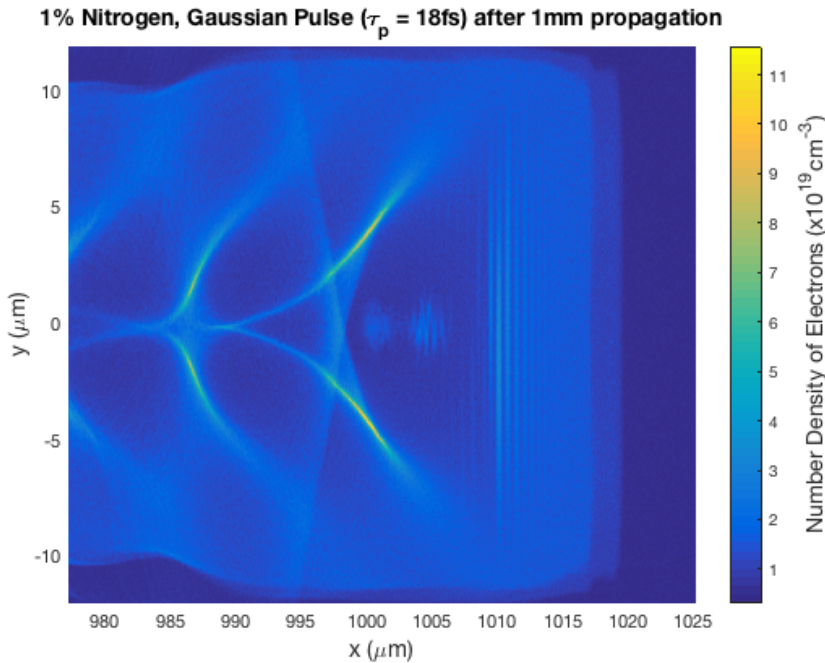


Figure 25: With a Nitrogen neutral number density of $n_N = 5 \times 10^{16} \text{ cm}^{-3}$ the blow out region and wakefield is still formed but now there is a noticeable bunch of trapped electrons. This is the accelerating region of the plasma density wave.

The larger amount of accelerated electrons with 1% Nitrogen compared with the negligible number injected using purely Helium in figure 31 demonstrates the viability of this injection method. The energy distribution is, however, very broad and this is due to electrons being injected continually along the acceleration length. If the injection method could be 'switched off', by having an injection region including the Nitrogen and an acceleration region being purely Helium, a monoenergetic bunch may be produced.

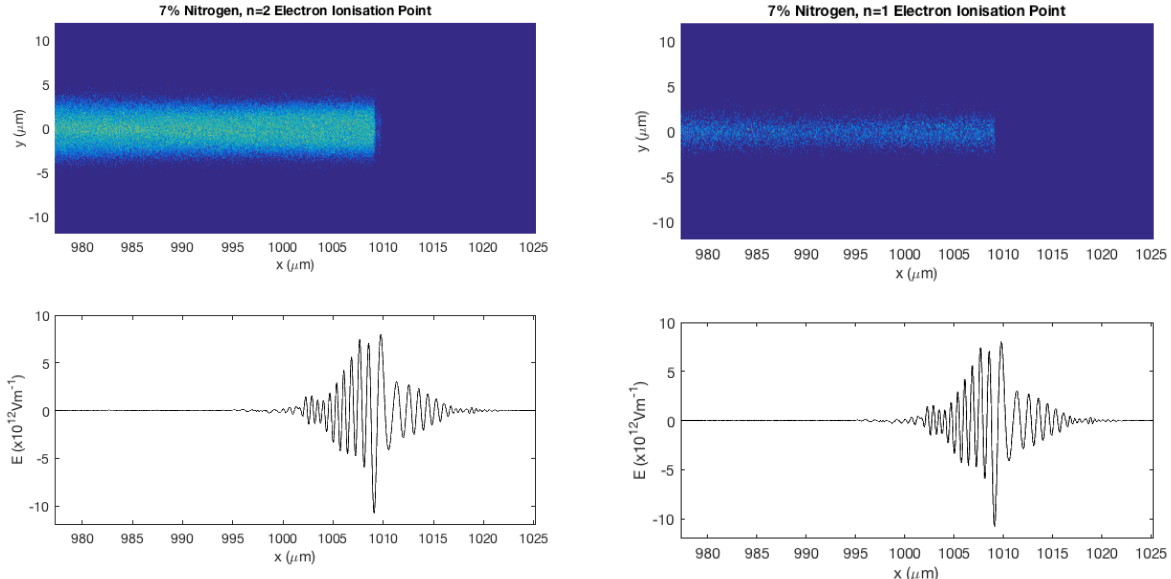


Figure 26: The $n=2$ electrons are ionised at the peak intensity of the Gaussian waveform. There is a large jump in the electric field and a departure from the Gaussian envelope due to the ionised electrons contributing to the electric field.

Figure 27: Similar to the $n=2$ electrons the $n=1$ and innermost, therefore most tightly bound, electrons are again tunnel ionised at the peak intensity. There are however noticeably fewer electrons and this is due to the increase in binding energy.

The location at which the two innermost electrons were tunnel ionised is shown in figures 26 and 27. These plots were produced using automatically generated electron species in the EPOCH code. As each electron is ionised it is labelled with an ordinal number, for example 'nitrogen6' would represent the sixth electron to be ionised. These tagged electrons then contribute to a species which can be extracted from the sdf files using Matlab. The two stacked plots 26 and 27 demonstrate the electron density plot of the $n=2$ and $n=1$ electrons of the Nitrogen and the complimentary electric field. In both of these cases neither of these tightly bound electrons are seen before the peak electric field amplitude. The $n=1$ case is particularly demonstrative in showing the tunnel ionisation. If, like the outer electrons, the inner two were barrier suppression ionised the number density would be the same for $n=1$ & $n=2$. The innermost electron has a noticeably lower number density and forms a much thinner line. This is because there is an even smaller region of the Gaussian profile in y for which tunnel ionisation becomes likely.

The concentration of Nitrogen was increased in steps of 1% to determine the number density at which the greatest amount of injection would occur.

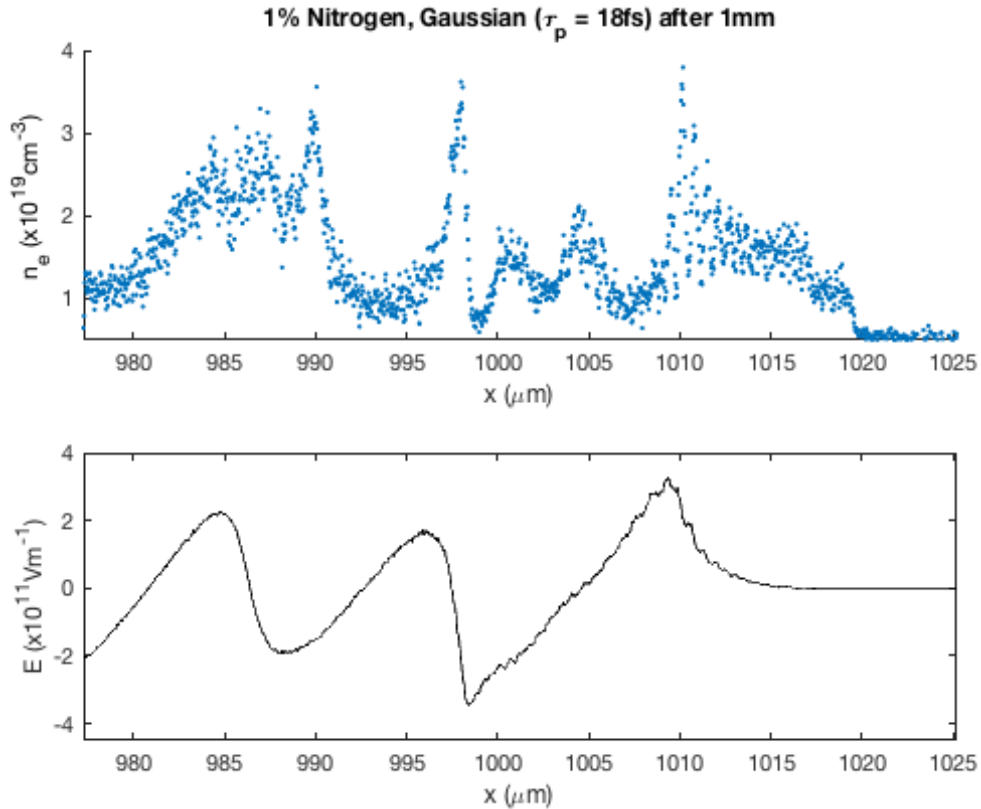


Figure 28: The denisty line out highlights that there are two bunches seen in the accelerating region. The electric field profile is also modified due to the presence of the electron beams.

There are two separate regions in which electrons are trapped in fig. 25 and the wakefield bubble has not formed the smooth circular profile seen in the pure Helium simulation. The Nitrogen electrons are increasing the number density and this coupled with the fact that the driving laser pulse was tailored to the plasma wavelength associated with the Helium number density (see pulse length variation 2) $n_{He} = 1 \times 10^{18} \text{ cm}^{-3}$ mean that the plasma is overdense. The addition of Nitrogen and the increase in He number density to $n_{He} = 5 \times 10^{18} \text{ cm}^{-3}$ will mean that more electrons are available to form the plasma altering the electron number density dependent plasma wavelength and so prevent the ideal bubble from forming.

The limits of acceleration were introduced in 1.4.1 and one of the most problematic effects was that of electron dephasing. The electrons are accelerated by the strong electric field of the wake so they become ultra-relativistic and hence have a velocity which is very close to the speed of light, $v_e \sim c$. The speed of the laser pulse in the plasma will be limited by the refractive index in the medium $v_\phi = c/\eta$. The refractive index of the plasma is electron number density dependent and can be written in terms of a ratio with the critical electron number density (n_c) [2], this is the density at which the plasma becomes overdense and an EM wave will not propagate. The critical density can be found by rearranging equation 16.

$$\eta = \sqrt{1 - \frac{n_e}{n_c}} \quad (42)$$

The lower the plasma density the faster an electromagnetic wave will propagate in the medium. With the addition of the Nitrogen neutrals, which will give up at least five electrons each, the plasma density was increased. This in turn caused the refractive index to become larger and so the laser pulse cannot

travel as quickly in the higher density plasma. The accelerated electrons however still move with approximately the speed of light and so catch the laser pulse more quickly. Dephasing occurs once the electrons move out of the accelerating region and get close enough to the drive laser to interact with its magnetic field. The effect is demonstrated in fig. 29 as the electrons are visibly oscillating in the field. In order to reduce this and increase the acceleration length a lower electron density must be used.

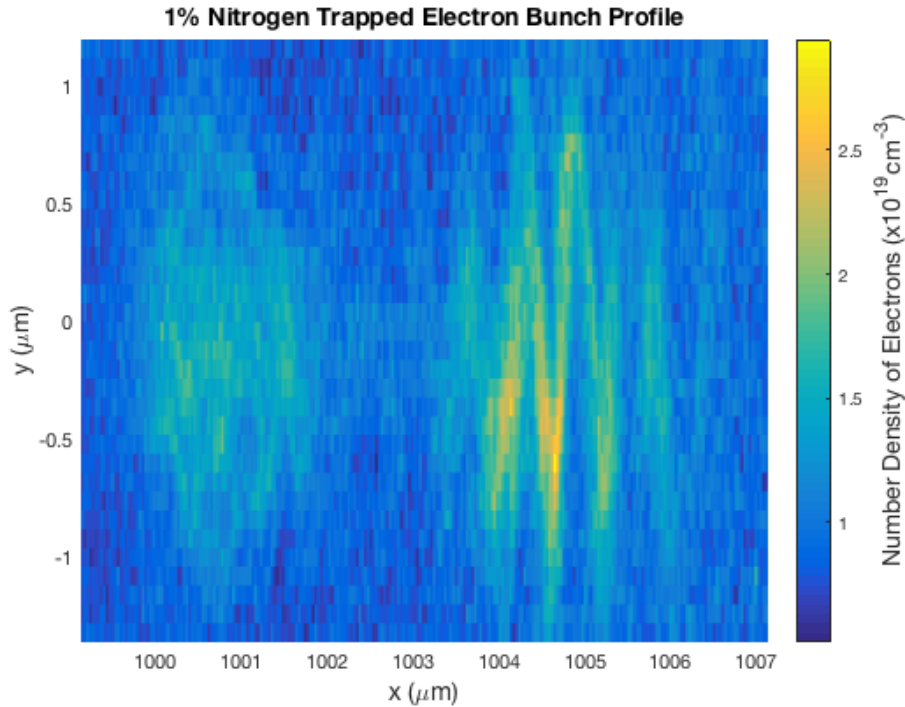


Figure 29: A closer view of the trapping region and the two distinct bunches therein. The trapped electrons sitting further forward are oscillating in the laser field.

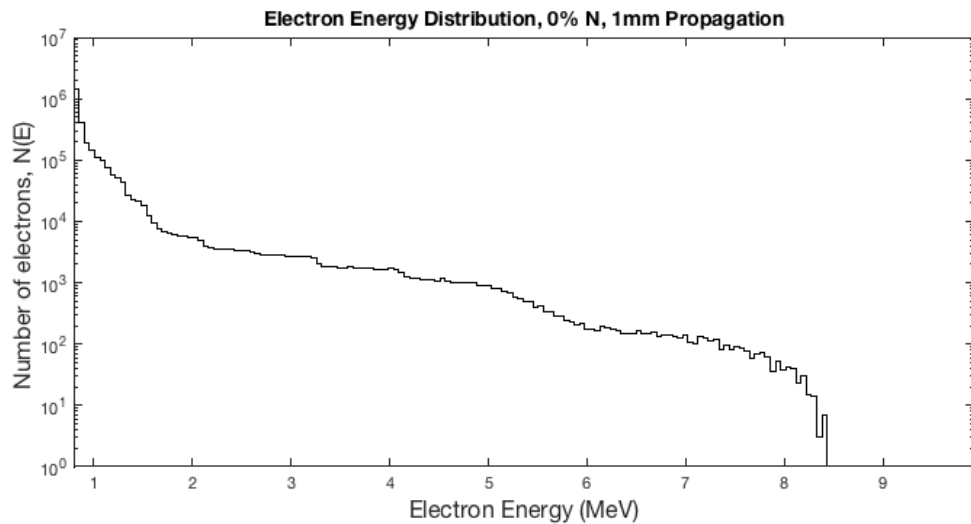


Figure 30: The energy distribution of the electrons in pure Helium plasma. This distribution illustrates the low energy spread of the electrons which produce the wakefield structures. There are a negligible number of electrons accelerated to higher energies.

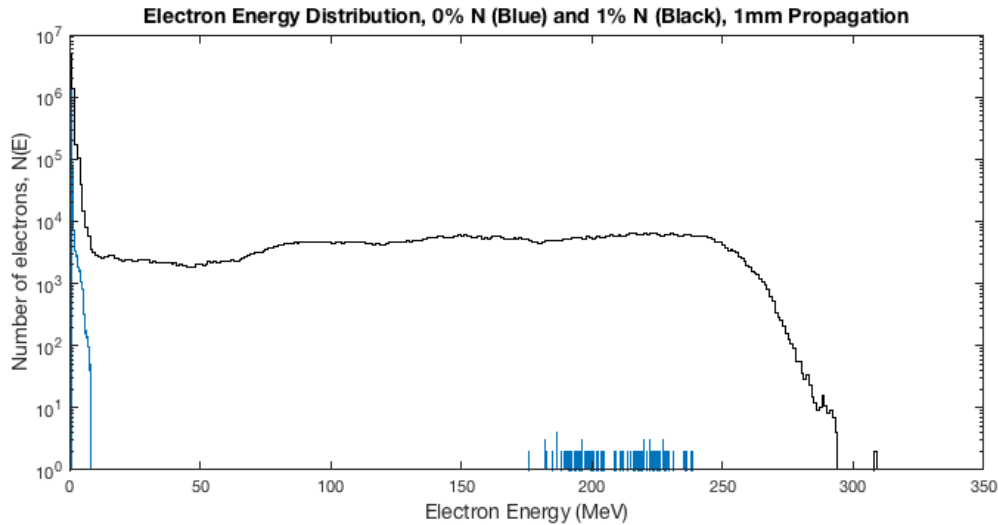


Figure 31: A comparative plot showing the vast increase in accelerated electrons even with 1% of Nitrogen relative to the Helium number density ($n_N = 5 \times 10^{14} \text{ cm}^{-3}$). The Helium electrons are of low energy with a negligible number accelerated. The addition of Nitrogen produces a considerable number of high energy electrons up to 250MeV.

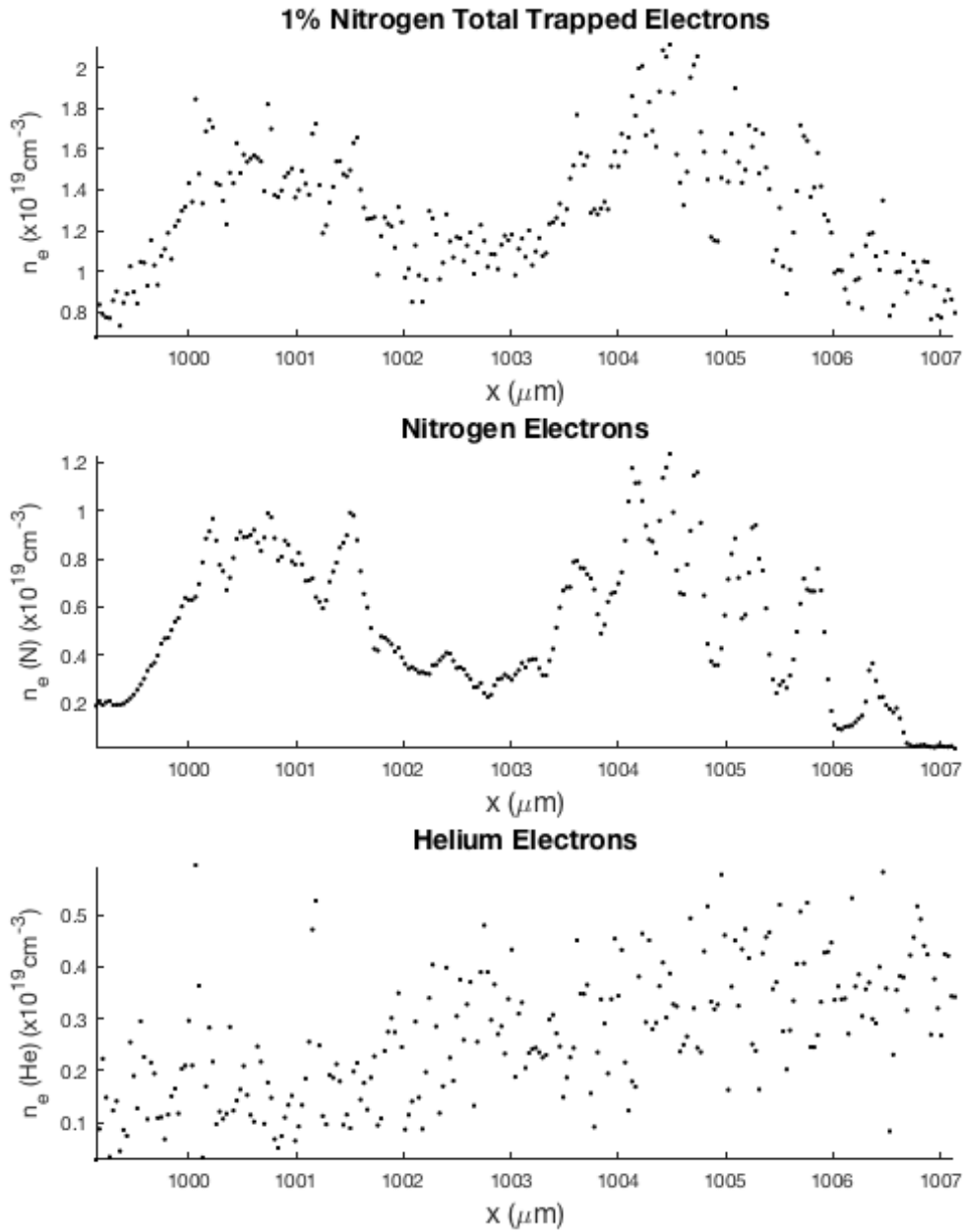


Figure 32: *Relative electron trapping, these line outs were produced from the close up electron bunches of fig. 29. The Nitrogen electrons contribute overwhelmingly to the bunch profile. The Helium electrons appear to have no contribution and sporadically appear across the region with the only discernable pattern being that their number decreases towards the rear of the trapping region.*

Closer inspection of the bunches in figure 29 demonstrates that the Nitrogen is responsible almost entirely for the accelerated electrons. The overall number density is compared to the Nitrogen and Helium contributions in figure 32. The Helium electrons are contributing to the wake structure as they are ionised at lower intensities of the pulse and so experience the longest exposure to the ponderomotive force. The electrons ionised earliest are then the ones that will be blown out to form the bubble structure. The more tightly bound electrons, being ionised near the peak intensity of the laser pulse, will not be exposed to the ponderomotive force long enough to blow out. These electrons are accelerated by the electric field from the plasma density perturbation but are sliding back through the wave. If the electrons gain enough energy they may move along with the density wave and continue to gain energy until one of the limiting conditions halts the acceleration.

In order to compare the amount of electrons in each bunch the density profile, at the varying concentrations of Nitrogen relative to Helium were used to find a peak number density. This number density was then plotted against the Nitrogen number density and figure 33 was the result.

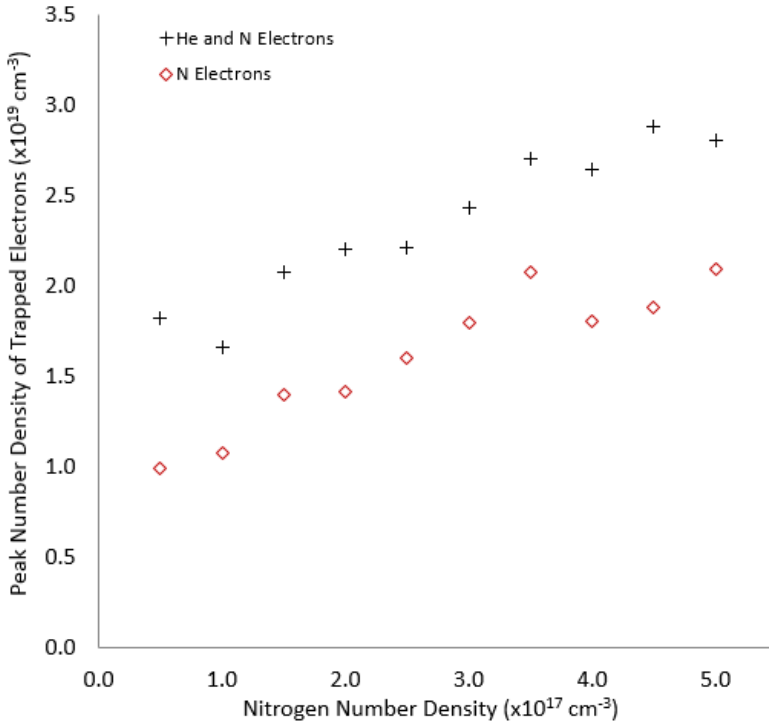


Figure 33: *The trapping of electrons increases linearly with Nitrogen concentration. The black crosses represent the total electron trapping, that is, from He and N. The hollow red diamonds denote the N electrons alone. This figure shows that the N electrons are the main source of the electron injection (see figure 32). These peak density values are from the left hand bunch visible in figures 32 & 29.*

The peak number density in the stable accelerated bunch (the left hand bunch which is not dephasing) is increasing linearly with N concentration although there are signs of plateau between 9% and 10%, however, this would require further investigation into higher concentrations still. Figure 34 shows a similar plot for the peak number of electrons in the dephasing region (see fig. 29, oscillating density profile interacting with the laser). The Nitrogen electron acceleration replicates the total trapping very closely which again indicates that this injection method is viable and the slightly higher atomic number neutrals contribute greatly to the electron injection.

The peak number density of electrons in the dephasing region (fig. 34) jumps dramatically with only a small increase in Nitrogen number density from $n_N = 0.5 \times 10^{17} \text{ cm}^{-3}$ to $n_N = 1.0 \times 10^{17} \text{ cm}^{-3}$ and after this point remains fairly constant with perhaps a slight negative slope. The relativistic electron dephasing expression (eq 31) taken from Esarey et al 2009 [8] reveals that the dephasing length is directly proportional to the cube of the plasma wavelength. The dephasing length is very sensitive to any change in λ_p . The plasma wavelength is inversely proportional to the square root of the number density ($\lambda_p \propto 1/\sqrt{n_0}$) meaning that any increase in number density will affect the dephasing length considerably by decreasing the plasma wavelength which in turn shortens L_d . This suggests that even the slight increase in number density caused by the introduction of Nitrogen neutrals, while increasing the number of injected electrons, has a significant contribution to the plasma parameters.

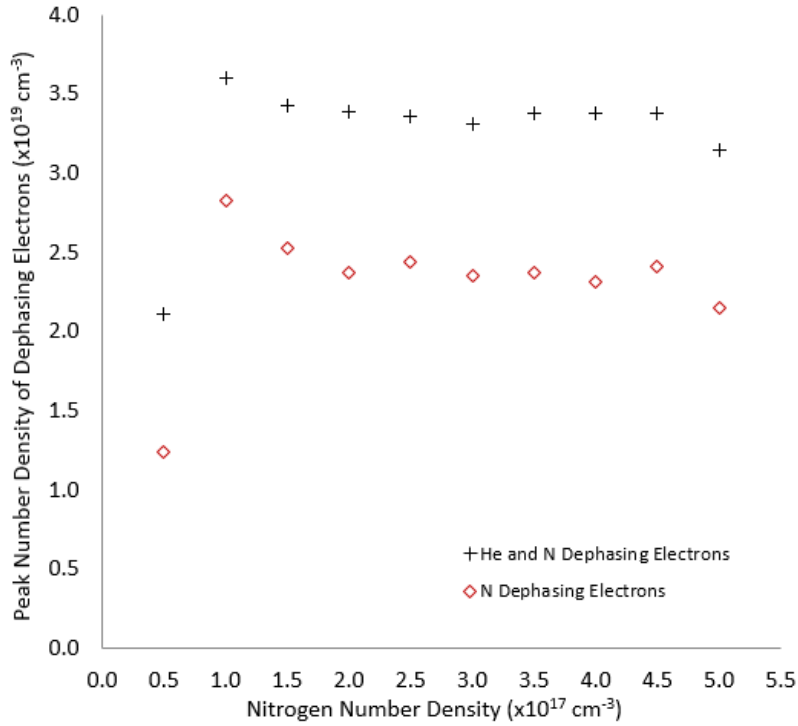


Figure 34: The peak number density of the dephasing region, this can be considered as electrons being decelerated due to dephasing. The dephasing peak number density jumps considerably from 1% ($0.5 \times 10^{17} \text{ cm}^{-3}$) to 2% ($1.0 \times 10^{17} \text{ cm}^{-3}$).

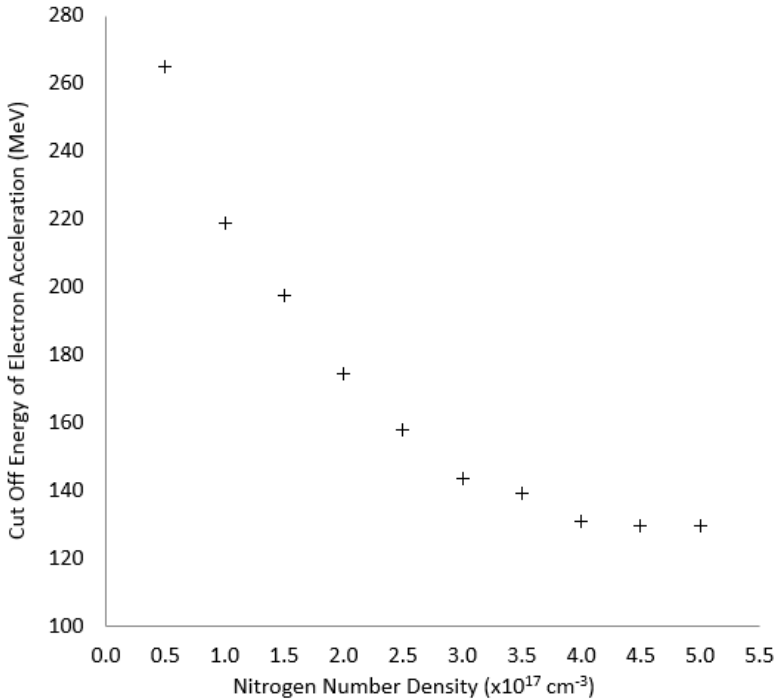


Figure 35: The energy at which the number of electrons fell below 10^3 in the electron energy distribution plots (see fig. 31) was recorded for each of the N densities and presented here. See table 55 for the full data set.

Evidence for the sensitivity of the electron bunch quality to any change in n_e is further strengthened by the plot in figure 35. A cut off electron count was taken to be 10^3 on the logarithmic scale of the energy distribution plots (fig. 31). At this point for each concentration the energy of the electrons was recorded and plotted against the Nitrogen concentration in the form of a number density. A clear inverse trend is observed for the energy as the number density of Nitrogen increases with the energy reaching a plateau around 130MeV. This could be the result of restrictions imposed by the increasing presence of Nitrogen and the many electrons each atom will contribute to the plasma state. The electron bunch quality would be improved for each concentration if the laser pulse was tailored to an estimate of the plasma density.

3.2.2 Reduced Density ($n_{He} = 1 \times 10^{18} \text{ cm}^{-3}$)

The number density was lowered so that the plasma wavelength was closer to the pulse length and the resonance condition $L \simeq \lambda_p$. The amount of injection and the energy spectra were simulated for a sample of Nitrogen number densities (1%, 5% and 10%)

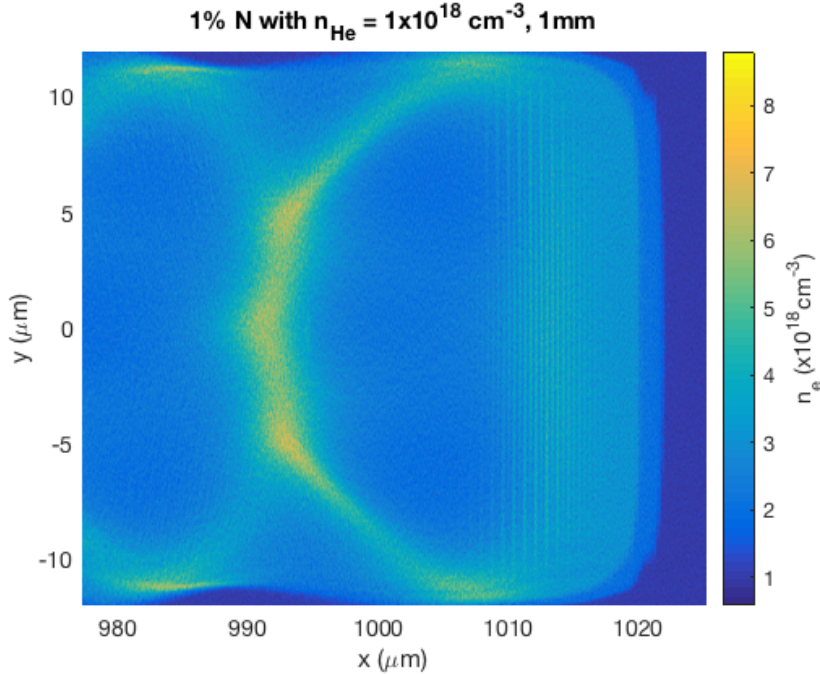


Figure 36: The lower Helium density forms a more complete bubble and there is a small amount of injection in a small bunch for this 1% Nitrogen simulation ($n_N = 1 \times 10^{16} \text{ cm}^{-3}$).

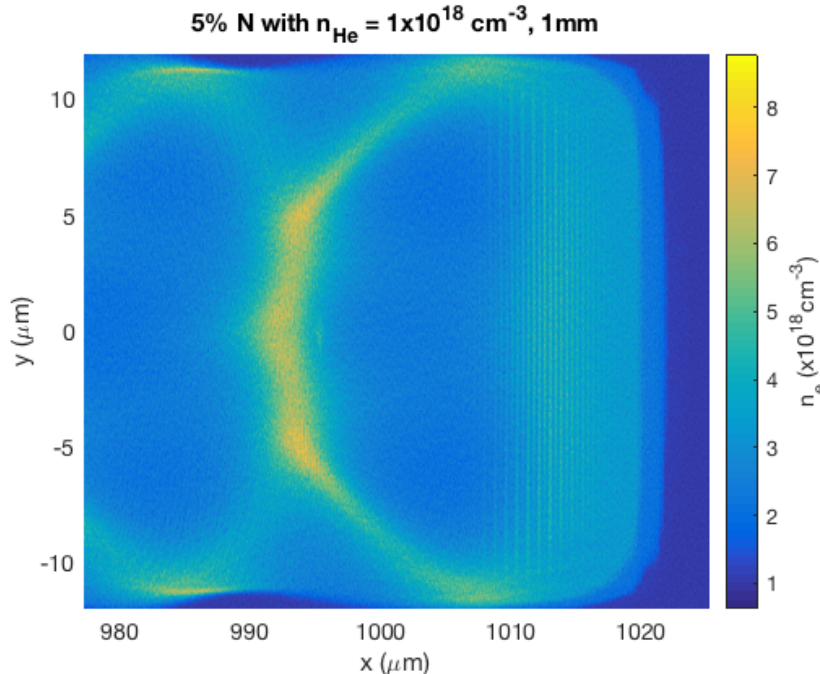


Figure 37: With an increase in n_N a stable bubble is still formed and there qualitatively appears to be more electrons injected.

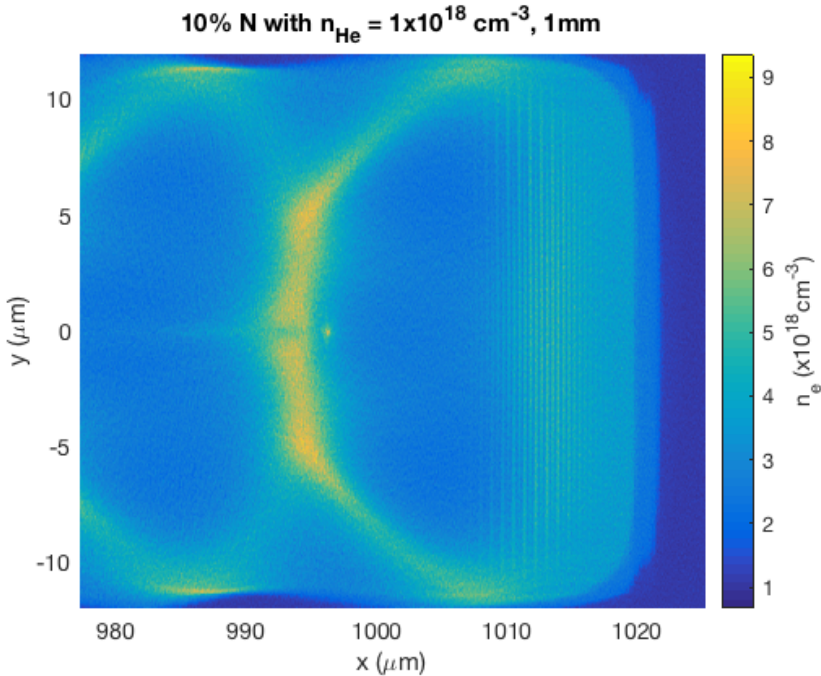


Figure 38: The 10% system shows a very prominent electron bunch which appears to be well collimated and coherent.

The lower electron density allows the pulse to form a more stable accelerating wake in comparison to the overdense case and this enables the formation of a very localised bunch. The lower density allows the EM wave to propagate at a higher velocity than the high density case and this is due to the density dependent refractive index in a plasma. The electron bunch has not caught the drive pulse and so the dephasing seen in fig. 29 has not occurred. The dephasing length has therefore been increased. Figure 55 demonstrates that the Nitrogen electrons in this case are not the main source of injection although there is an order of magnitude decrease in injection compared to the $n_{He} = 5 \times 10^{18} \text{ cm}^{-3}$. The Helium electrons are contributing to the acceleration region although the increasing number density behind 996 μm suggests that the majority of the electrons are slipping back through the acceleration region and forming the wakefield structure.

The electron energy spectra for each of the concentrations display a commonality in that they each have the low energy wake forming electrons and a separate population of accelerated electrons. The vast majority of the electrons involved in the laser plasma interaction contribute to the wakefield. Each of the distributions then has a separate higher energy feature, which is likely to be the trapped electrons. Figure 41 is the energy spectra for 10% Nitrogen and the other two simulated concentrations (1% & 5%) have the same trend. These higher energy regions have a sharp cut off and the energy cut off increases with Nitrogen number density. While the higher energy bunches for the $n_{He} = 1 \times 10^{18} \text{ cm}^{-3}$ case have a smaller spread than the more dense plasma (see fig. 31) the number of electrons at these higher energies is two orders of magnitude less, or 100 times less as can be seen in figure 39.

$n(N) (\times 10^{16} \text{ cm}^{-3})$	N (%)	Energy Cut Off (MeV)	Number of Electrons
1.0	1	144.0	12
5.0	5	152.0	36
10.0	10	163.0	30

Figure 39: This table records the cut off energies for the lower density plasma, $n_{He} = 1 \times 10^{18} \text{ cm}^{-3}$. The cut off energy is increasing with the increasing Nitrogen number density but the number of injected electrons is considerably smaller for this lower density system.

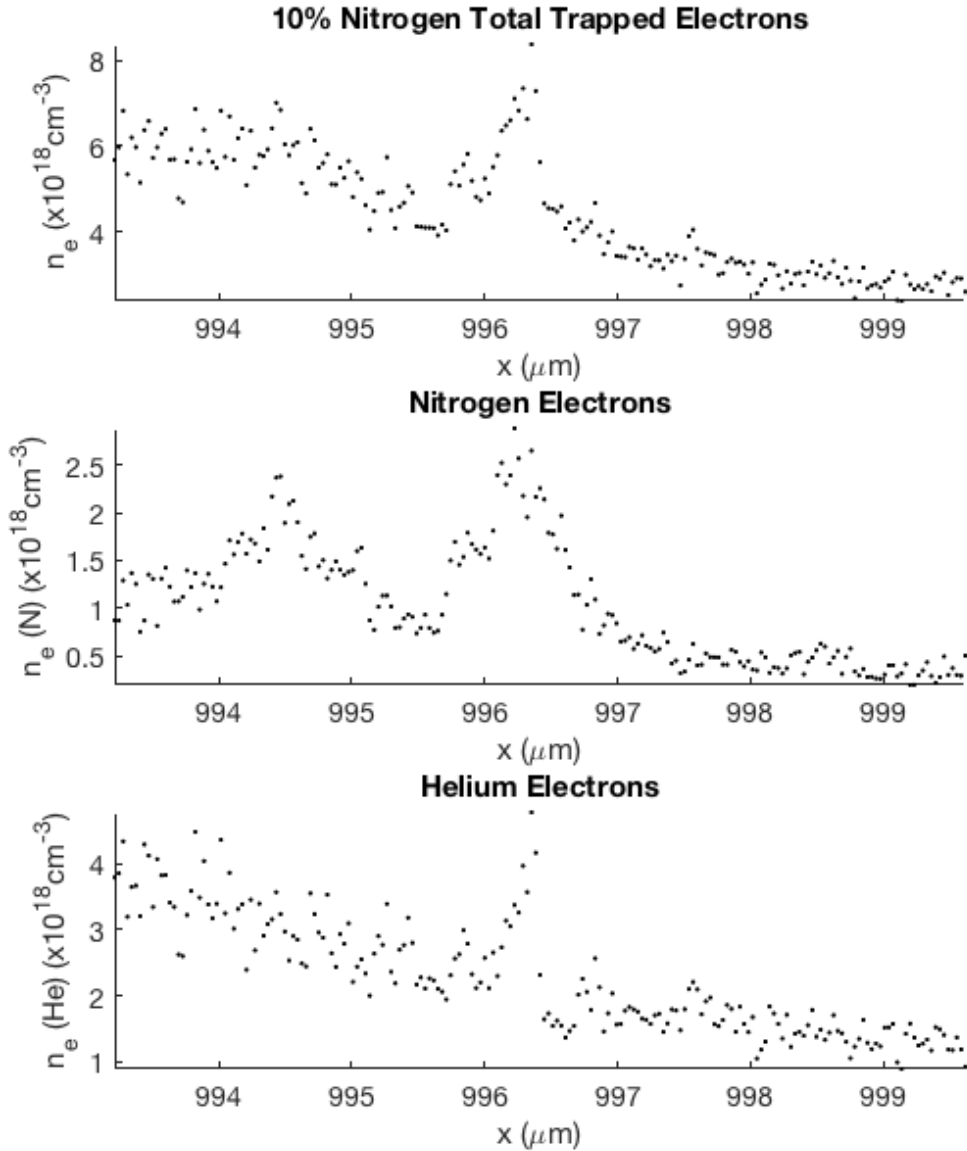


Figure 40: The well defined injected electron bunch is clearly visible just ahead of the 996 μm point on the x axis in the top total electron number density lineout plot. The Nitrogen electrons as before follow the same trend and appear to give a large portion of the electrons to the bunch. The Helium line out, unlike the higher density plasma considered earlier, has a larger peak than the Nitrogen in the trapping area.

The $n_{\text{He}} = 1 \times 10^{18} \text{ cm}^{-3}$ system still demonstrated electron injection and acceleration but with a few differences. The electron bunch was much more concentrated and lower in number. There appeared to be no signs of dephasing limiting the acceleration so although the cut off energy was lower for the smaller Nitrogen concentrations than the higher density simulations. The cut off energy for 10% N was higher with a lower electron plasma density which is an interesting result.

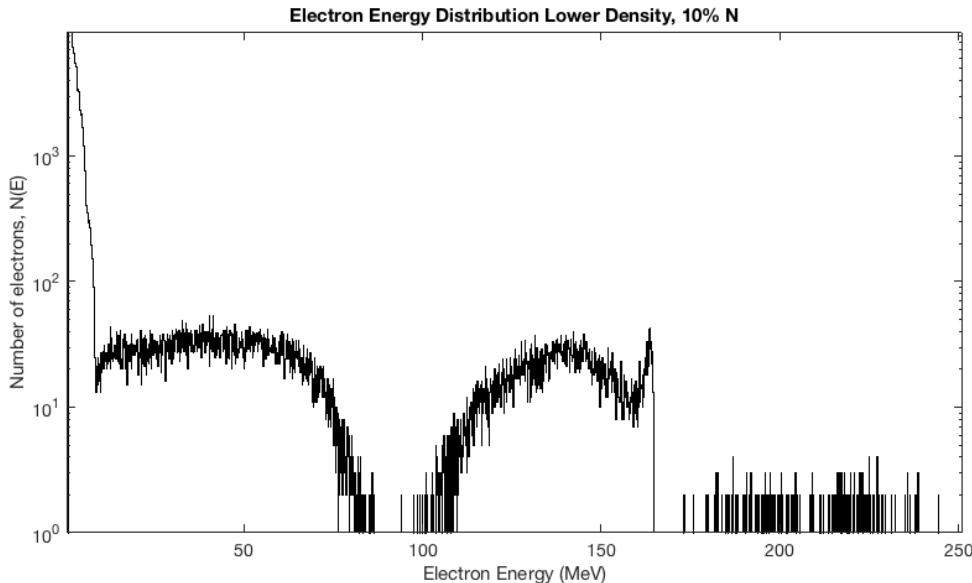


Figure 41: The energy spectra differ substantially from the higher density case seen above (fig. 31). The low energy wakeforming population is still present, although reduced in number. Instead of the broad high energy distribution seen in the $n_{He} = 5 \times 10^{18} \text{ cm}^{-3}$ there is a band of energy in which there are no electrons and beyond this exists a higher energy bunch.

3.3 Discussion

The introduction of Nitrogen neutrals vastly increased the amount of electron injection into the acceleration region and this in turn meant that larger numbers of electrons reached higher energies. The over-dense electron plasma number density demonstrated the largest number of injected and accelerated electrons, perhaps due to there simply being more electrons available after ionisation. The highest energy was also reached with 1% N at the higher density ($n_N = 0.5 \times 10^{17} \text{ cm}^{-3}$), 265MeV. With a larger plasma electron number density the energy distributions were broad and the electrons reached a higher energy quickly. The electron bunch also reached the dephasing limit much more quickly and this was caused by the laser propagating more slowly in the plasma, as a consequence of the higher electron number density, and the electron bunch was able to catch the drive laser. This put a limitation on the peak energy of the electron bunch and meant that if the system were allowed to continue the electron bunch would be completely destroyed and there would be only a small number of high energy electrons.

In order to increase the dephasing length, L_d , and so the distance over which the electrons could be accelerated the number density of the Helium and hence the electron plasma number density was reduced to $n_{He} = 1 \times 10^{18} \text{ cm}^{-3}$. The decrease in number density did increase the acceleration length as there were no signs of dephasing after the same distance of propagation. The number of injected and accelerated electrons was much smaller and for the lower density and the energy spectra showed that while the cut off energy of the 1% N higher density ($n_N = 0.5 \times 10^{17} \text{ cm}^{-3}$) was far greater than the same concentration relative to the lower He density ($n_N = 1 \times 10^{16} \text{ cm}^{-3}$). The highest concentration simulated demonstrated the reverse, with the 10% N in the higher density He ($n_N = 5.0 \times 10^{17} \text{ cm}^{-3}$) had a lower energy cut off compared to $n_N = 1 \times 10^{17} \text{ cm}^{-3}$ (10% in $n_{He} = 1 \times 10^{18} \text{ cm}^{-3}$).

In order to fully characterise the consequences of Nitrogen concentration a much more thorough investigation and while general trends have been identified here much more simulation is required in order to draw complete conclusions. The rest of the Nitrogen percentages at the lower density would need to be simulated first. After this is would be informative to calculate an estimate of the electron number density after the laser has ionised the neutrals (based on the assumption that the He contributes two electrons and the N at least five). With this estimation the plasma wavelength could be determined and then the laser pulse could be tailored to the resonance condition $L = \lambda_p$ for each of the concentrations.

4 Focussing Beam

The inherent limitations associated with plasma based electron accelerators are known and it is with finer control of plasma parameters and some ingenious techniques that these limitations may be stifled or removed altogether. The length over which the electrons can gain energy (section 1.4.1) is limited by several factors, one of which is the diffraction of the laser itself. During these simulations a collimated laser pulse has been used, and while this has produced the necessary results, such a beam is subject to this diffraction. Although electron dephasing has had a more prominent role in capping the peak energy of electrons for the Nitrogen trapping investigation (3). One of the simplest ways to reduce the effect of diffraction is to focus a beam properly. In the case of laser driven plasma accelerators it would be advantageous to focus the beam such that the dispersion inherent in the pulse were balanced with a long focal length which would act to increase the laser propagation distance in the plasma.

An input deck to produce a focussed Gaussian beam using the EPOCH code is developed in this section. A symmetric Gaussian will be considered, the lowest order spatial mode produced in a spherically symmetric cavity. Such a beam may be focussed down to a finite size.

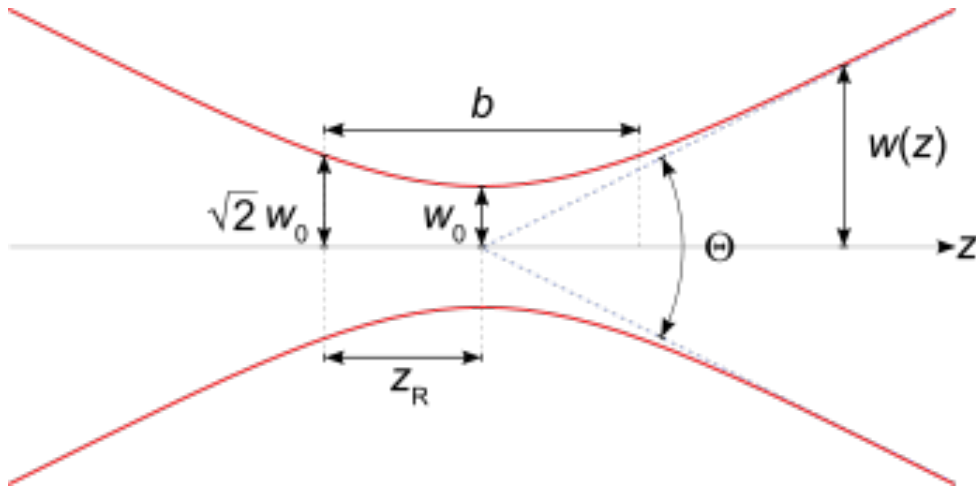


Figure 42: A Gaussian profiled beam will focus as depicted in this diagram. The beam focusses down to a finite waist size, w_0 . [21]

A beam with initial diameter D will focus to a finite waist size, w_0 over a focal length of f when focussed by an optic with that focal length. These three parameters are related by the following simple relation [22];

$$w_0 = \frac{2f\lambda_L}{\pi D} \quad (43)$$

In order to write an input deck a few important parameters must be defined. The Rayleigh length is the length over which the intensity of the beam will fall by a factor of 2, or the radius of the beam increases by a factor of $\sqrt{2}$ [23].

$$Z_R = \frac{\pi w_0^2}{\lambda_L} \quad (44)$$

Figure 42 shows this length graphically along with the related parameter, the confocal parameter (b) which is the distance between $\pm Z_R$.

A focussing beam is achieved using a radius of curvature which will evolve as the pulse propagates along with a Guoy phase term. The radius of curvature for a focussing Gaussian is as follows [22];

$$R(x) = x \left[1 + \left(\frac{Z_R}{x} \right)^2 \right] \quad (45)$$

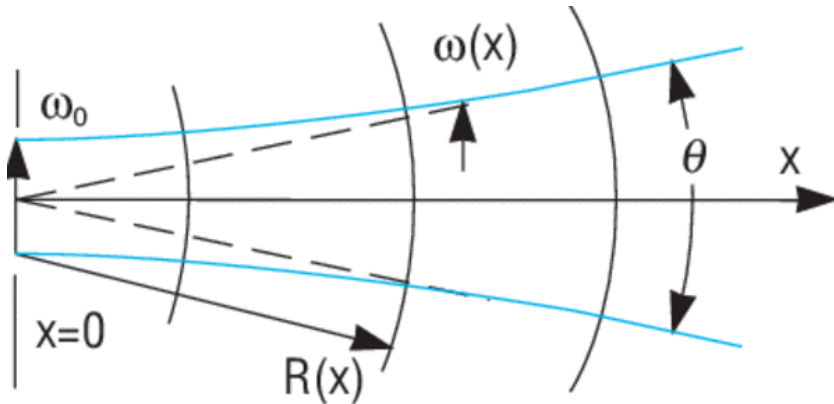


Figure 43: The radius of curvature after the focus of the beam. At the minimum waist radius the radius of curvature becomes infinite, becomes a straight line, but before and after it will evolve as described by eq. 4. [22]

Several sections of the radius of curvature are overlaid onto the beam waist profile in fig. 43. Another important consideration when modelling this system is how the beam waist will evolve (the light blue line in fig. 43). As the EM wave propagates along the x axis with a radius of R the waist size will be determined by [22],

$$w_x^2(x) = w_0^2(x) \left[1 + \left(\frac{x}{Z_R} \right)^2 \right] \quad (46)$$

The Guoy phase is the change in apparent wavelength and this increases near the beam waist and will be used to implement the focussing of the pulse.

$$\psi(x) = \arctan \left(\frac{x}{Z_R} \right) \quad (47)$$

Each of these relations were included into the input deck in order to produce a focussing beam.

4.1 Methods

Initially the focussing equations and parameters were tested in vacuum in order to demonstrate the viability of the input deck produced. This input deck was simply 6.1.4 without the particle species. The input deck was then a modified version of the electron trapping deck (6.1.3) used in section 3 once the focussing components tested in vacuum were added in. The constant values associated with Rayleigh length, the radius of curvature etc were inserted into the constants block.

```
begin:constant
lambda0 = 1.0 * micron
temp = 0.0
#speed of light
c_l = 2.99792458e8
#peak density of He and N neutrals
dens_max = 2e24

#Beam waist diameter size
D_0 = 10 * micron

#Radius of the beam waist
w_0 = D_0 / 2.0
```

```

#Focal length of the beam
f_x = 3.14e-4

#Rayleigh length
Z_R = (pi * (w_0)^2) / lambda0

#spot size evolution
W_x = (w_0) * sqrt(1 + (f_x / Z_R)^2)

#Radius of curvature
R_c = f_x * (1 + (Z_R / f_x)^2)

#Guoy phase determination
g_phase = atan(f_x / Z_R)
end:constant

```

All of the values necessary were calculated here before being used in the dynamic equations which were included in the laser block.

```

begin:laser
boundary = x_min
intensity_w_cm2 = 8.0e18
lambda = lambda0
pol = 0.0
phase = (2.0*pi/lambda0) * (y^2/(2.0*R_c))
- g_phase
profile = gauss(y,0,W_x)
t_profile = gauss(time,52*femto,26*femto)
end:laser

```

The machinery of the focussing itself is controlled by the phase components in the laser input deck and the waist profile. This can be thought of as spot size evolution and is included in the 'gauss' command discussed in [1.5.1](#). A phenomenological test of the focussing deck was first simulated in order to compare the electric field structure to a beam with the same parameters without the suite of focussing equations.

In order to capture the evolution of the beam focussing the simulation box parameters had to be modified with increased resolution in the y axis so that the changing electric field profile would be resolved as the beam converged to its focal point. See the full input deck for the exact simulation region specifications, [6.1.4](#).

4.2 Results

The focused beam was set to have the following parameters in the constants block of the input, these parameters were calculated using the simple relations in [4](#) along with the laser parameters. The input deck section in the appendix ([6.1.4](#)) details the complete settings and deck structure.

The laser parameters were as follows;

$$\begin{aligned}\lambda_L &= 1\mu\text{m} \\ I_0 &= 8 \times 10^{18} \text{ W cm}^{-2} \\ \tau_L &= 26\text{fs}\end{aligned}$$

And the calculated focussing parameters are;

$$w_0 = 5\mu\text{m}$$

$$f_x = 314\mu\text{m}$$

$$Z_R = 78.5\mu\text{m}$$

$$R_c = 0.334\text{mm}$$

The testing of the focussing method began with the Gaussian in time and space laser pulse focussing according to the above conditions. The data is presented as the electric field variation along the y direction, the plots show the simulation box with a 3D surface plot overlaid. This 3D surface is seen from above and the electric field strength is represented using smooth contours quantified by the colour bar. As the beam entered the simulation box the curved phase fronts could be easily observed, figure 44.

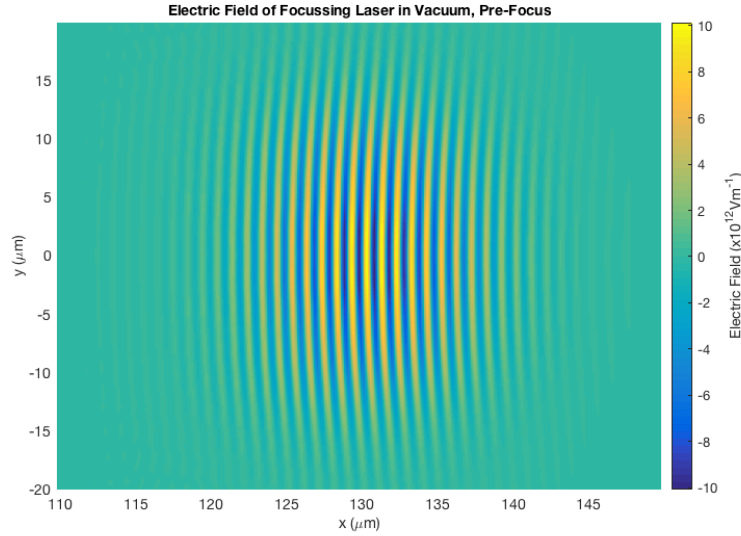


Figure 44: The concave phase fronts which regulate the focussing are discernable within the pulse envelope. This is the electric field distribution in y before the minimum waist size is reached.

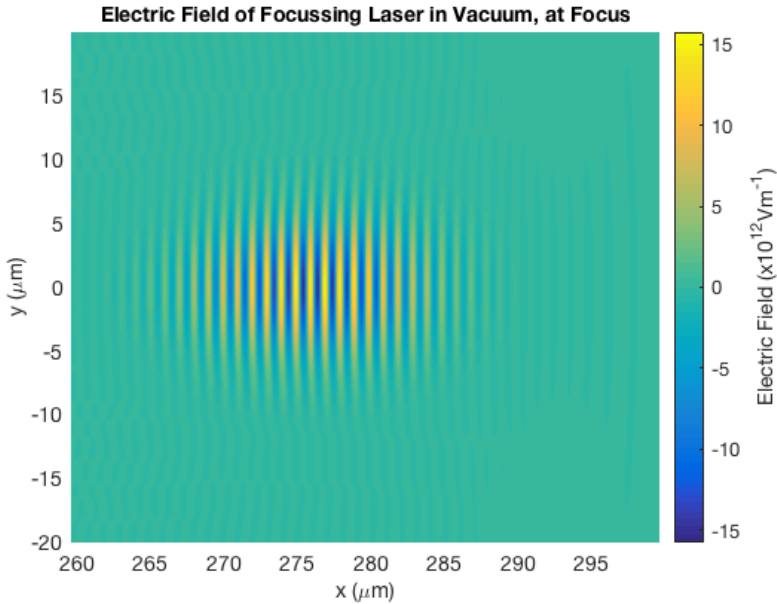


Figure 45: The focal length, as listed above, is $314\mu\text{m}$ and so this snapshot is slightly before the minimum waist size. The electric field plot still demonstrates the relevant behaviour.

Near the focal point as in figure 45 the laser is contained in a small volume and as such has its highest intensity at the focal point. The radius of curvature for the wavefronts has increased and will continue to increase up to an infinite radius of curvature at the focal point. The infinite radius of curvature corresponds to a flat wavefront, this then turns over and the phase fronts become curved in the opposite direction. Now as the pulse moves away from the focal points the radius of curvature decreases and so the pulse spreads out in space and diffracts as in figure 46 and this agrees with the theoretical diagram showing wavefront form after the focal point (fig. 43).

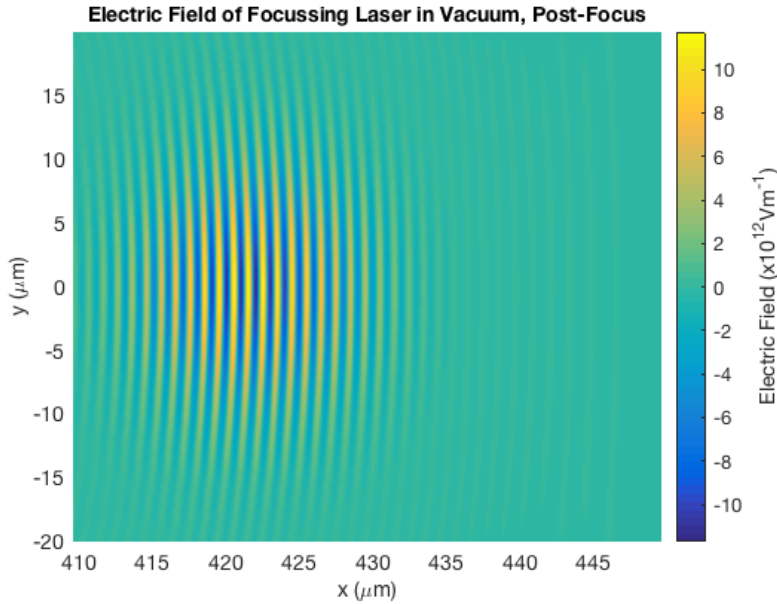


Figure 46: Once beyond the focal length the curvature increases again as the pulse diffracts. The energy of the laser continues to occupy a larger and larger volume causing the intensity to decrease.

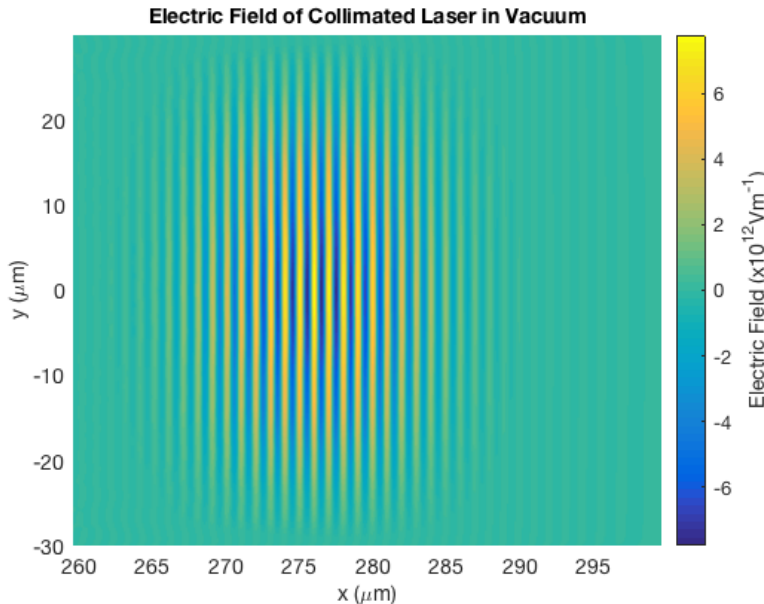


Figure 47: With none of the phase space and waist profile altering equations the pulse is a simple collimated ray. Such a wavepacket is still subject to diffraction limitations.

A collimated beam, such as the one used in previous sections, will not demonstrate any of these features but simply move with a constant spatial profile. The collimated ray in figure 47 shares all the same parameters as the focussing beam but without the variation in phase and waist profile. The collimated beam then has no curvature to the phase fronts and propagates with a constant spatial envelope.

The focussing pulse is of use in plasma based electron accelerators as the collimated ray will suffer diffraction in a medium and the focussed beam can be used, if the parameters are set correctly, to extend the acceleration distance. This is done by using the focussing of the laser to balance against the diffraction effects of the plasma medium. This does require that the total angular spread be small (Θ in fig. 42). A small angular spread will mean a slowly focussing laser and a long Rayleigh length (Z_R) and this is ideal for increasing the diffraction limit, L_d (1.4.1).

The same focussing parameters were used to produce a beam focussing in the distribution of neutrals identical to the 6% Nitrogen set up in section 3. The next set of results show the detrimental effects that a rapidly focussing beam will have on any laser wakefield system. Such a pulse will have a very short Z_R and so diffract extremely quickly after the focal length. Figures 48, 49 and 50 depict the system before, at and after the laser focus respectively. The comparative plots; figures 51, 52 and 53 demonstrate the collimated pulse at the same intervals.

Each plot in this data set is presented as a double stacked figure, the top plot details the number density distribution as has been seen throughout the report. The lower sub-plot is the same smooth contour surface plot of the electric field in x . Both are quantified with a colour bar on the right hand side of each figure.

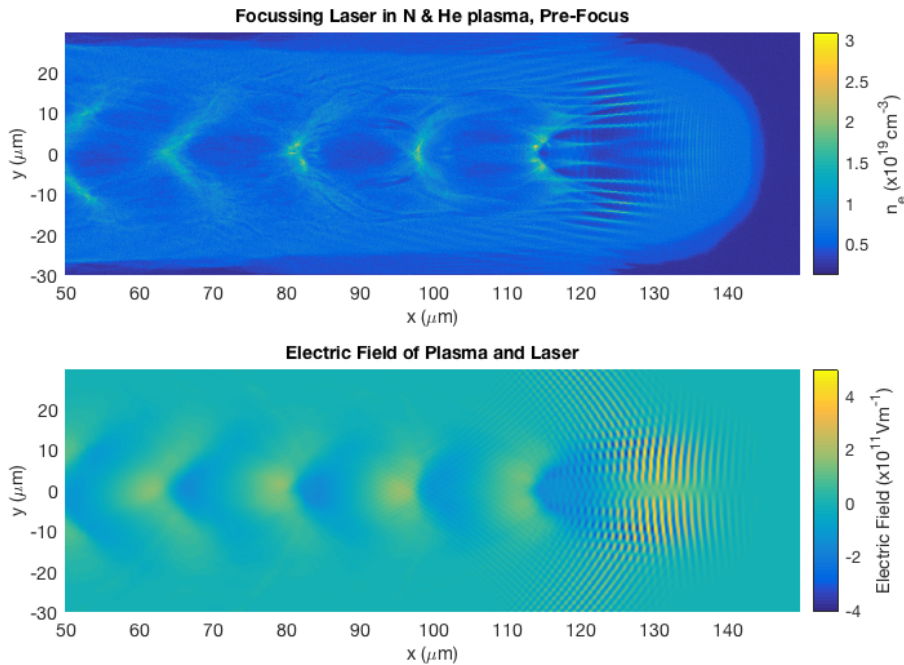


Figure 48: The focussing EM wave has begun to form a blow out region and there is a well defined pulse train. The beginnings of electron injection are identifiable in the number density plot.

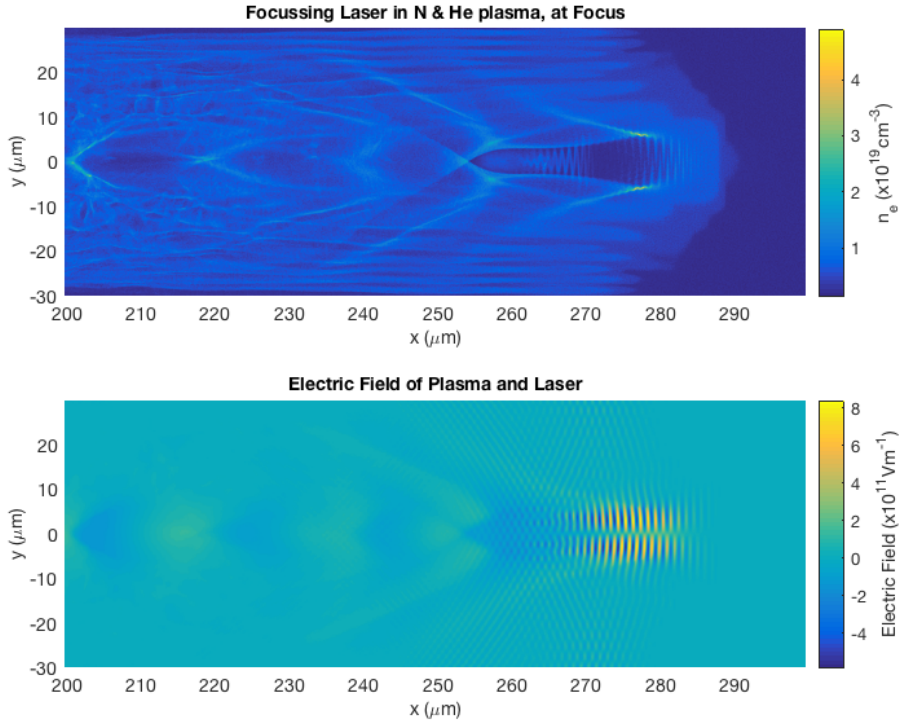


Figure 49: Around the focal length the electric field profile of the Gaussian has narrowed considerably and is approaching the waist radius. The electric field strength has increased as the envelope is compressed into a smaller volume. The density plot demonstrates an elongated blow out region and there is electron injection, likely from the Nitrogen neutrals (see 3). There is a large amount of dephasing as the trapped electrons oscillate in the field of the focussed laser.

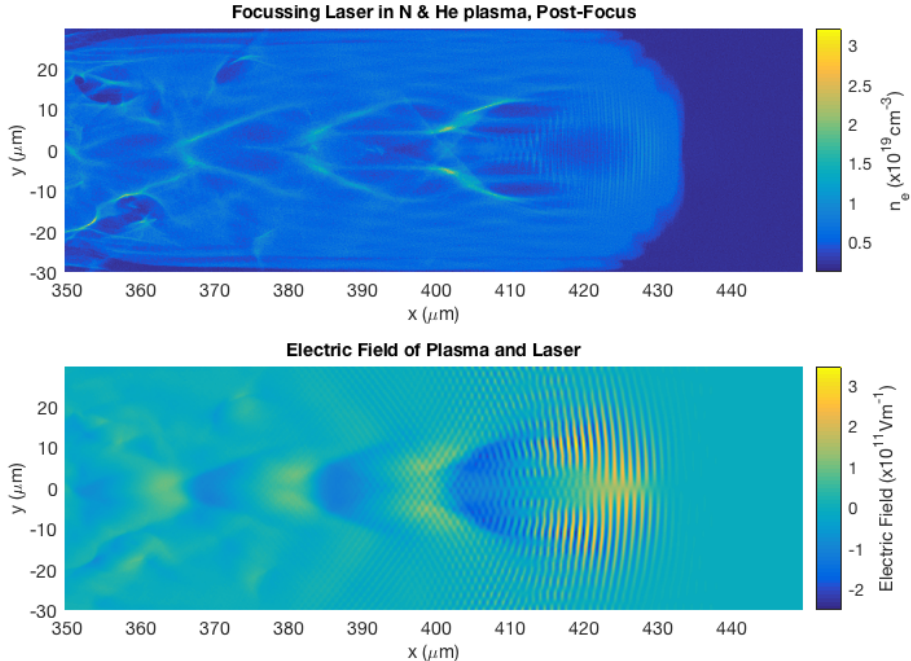


Figure 50: Shortly after the focal length the beam has already begun to diverge very quickly. This is due to the short focal length of the pulse, which was chosen to show the pulse evolution over short scales. The density profile still exhibits dephasing and there are still electrons being accelerated. The electric field plot demonstrates the expanding envelope and the decrease in electric field strength after focus.

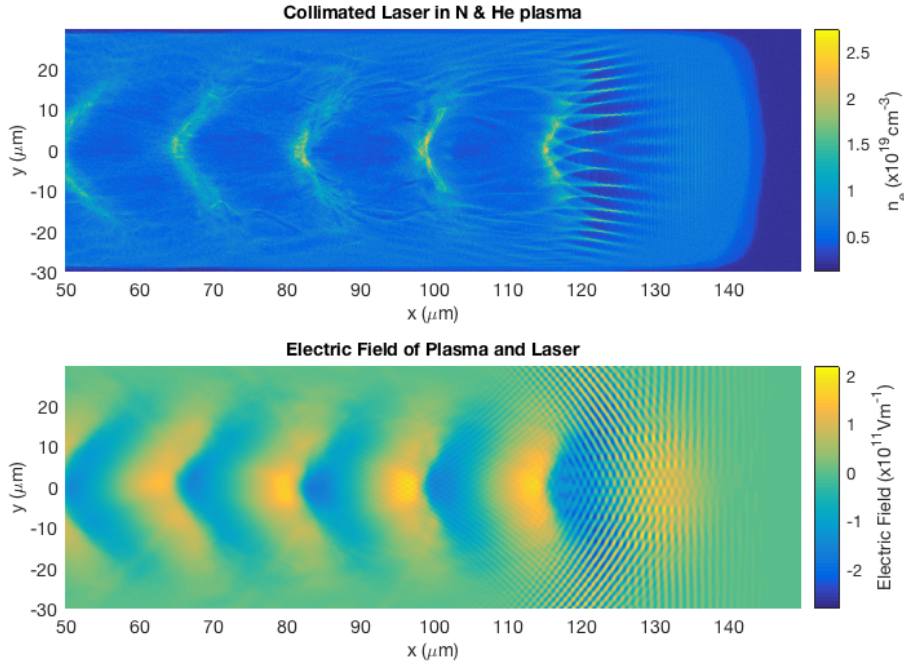


Figure 51: The collimated ray demonstrates a similar behaviour to the focussing beam at this early stage of the systems evolution. The pulse train has formed and the blow out region is beginning to show signs of electron injection.

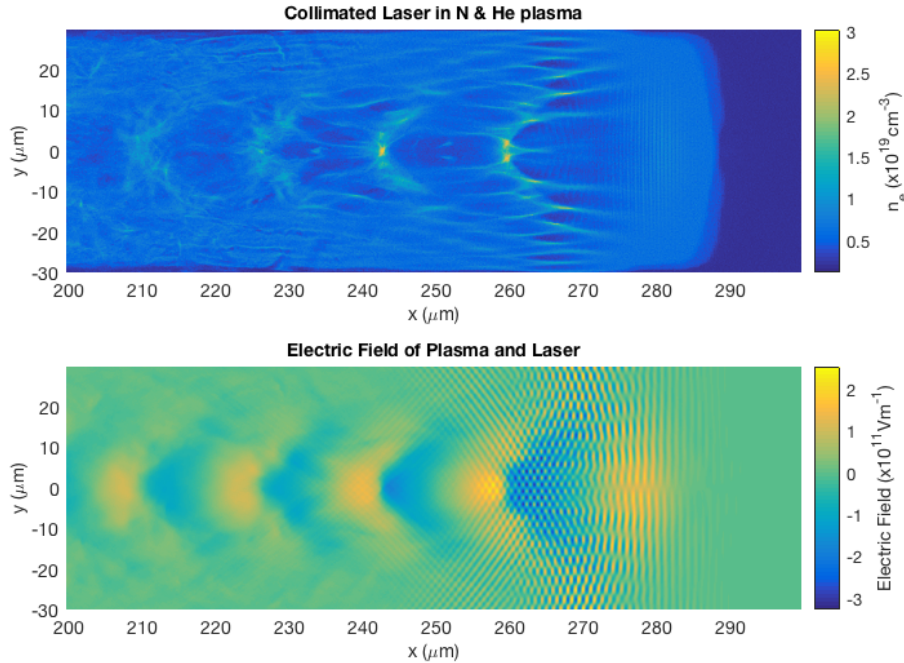


Figure 52: At the same point at which the converging pulse would have almost reached its minimum waist radius the electric field profile of the collimated ray has remained fairly constant, as expected. There is a visible level of electron injection in a collimated electron beam with much less electron dephasing.

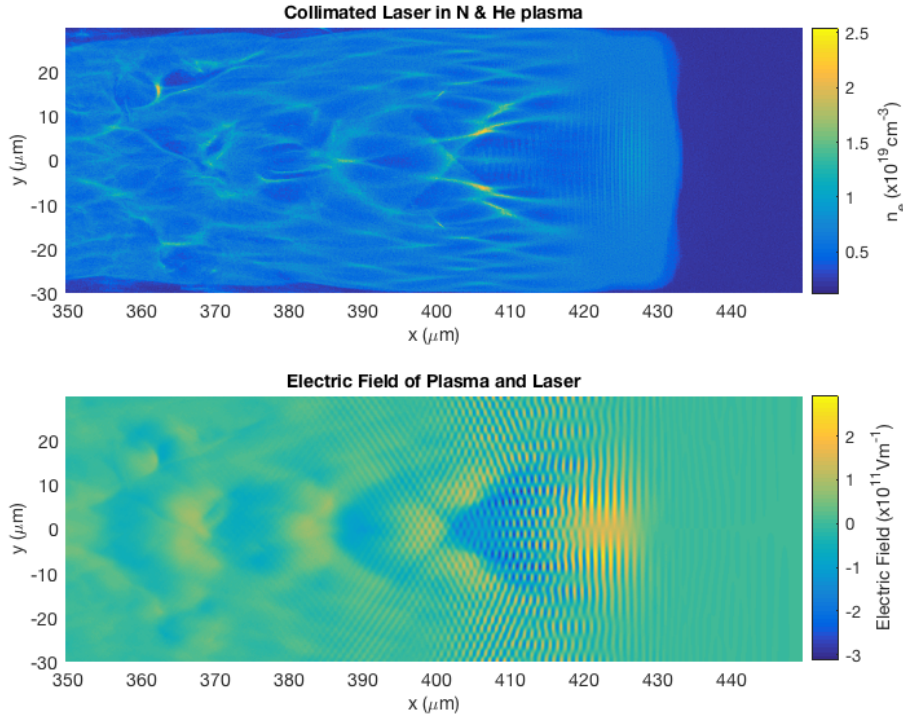


Figure 53: The electric field strength is reducing due to pump depletion (the laser pulse using its energy in driving the plasma wake). However, there remains a trapped electron bunch.

After 140 μm the bubble has partially formed for the focussing case (fig. 48) along with the train of wakes and this is similar to the collimated simulation (fig. 51). The pre-focus system demonstrates the beginnings of coherent electron trapping and the formation of an electron beam and while the constant spatial profile shows signs of trapping there are still instabilities (multiple electron streams ahead of primary wake). As the pulses continue to propagate toward the focal length, the bubble region of fig. 49 has narrowed considerably and there are injected electrons. A large amount of electron dephasing is apparent as the front of the electron bunch interacts with the pinched and elongated field. Conversely the constant Gaussian laser has injected electrons and is maintaining a collimated electron beam with no dephasing (fig. 52).

After focus the pulse (fig. 50) has diffracted rapidly and the injected electrons are, on the whole, dephasing. The blow out regime has become unstable. This is partially due to the plasma being overdense causing an incomplete bubble. The rear of the blow out region is not connected, forming a smooth curve wake, but separated and smeared out. Double electron jets appear to have formed either side of the oscillating pattern of the dephasing electrons. In the collimated beam there are signs of the overdense plasma causing dephasing but the injected electrons are still in a well collimated bunch and propagating with the laser.

4.3 Discussion

These comparative graphs demonstrate the negative effects that a rapidly focussing beam will have on the laser wakefield system. While electron injection was achieved in a shorter time scale the additional instabilities introduced by the rapidly focussing beam greatly reduced the length over which a stable electron bunch could be accelerated. The dephasing length was the primary factor in reducing the acceleration length. The electron number density and E-field diagrams revealed that as the pulse approached the minimum waist radius the electric and magnetic field influence of the laser stretched back into the trapping region and this vastly increased dephasing effect.

In order to demonstrate the usefulness of this technique in optimising electron acceleration simulations with slowly focussing laser pulses must be performed in less dense plasma. The slowly varying

spatial envelope would counter the diffraction effect of the plasma medium and allow for an increased electron acceleration length. With a less compressed waist the fields of the EM wave may not have such an interfering influence on the trapping region but this is conjecture and would require further simulation.

5 Discussion and Conclusions

During this report several aspects of laser wakefield accelerators have been considered. In section 2 the effect of altering the pulse length and temporal profile were considered. This investigation was able to determine that there existed a resonance condition for which the blow out region and amplitude of the wake were both vastly increased. With pulses which were either too long or too short compared to the plasma wavelength the bubble was either not formed or had a large amount of instabilities. Along with this resonance condition the simulations were able to highlight that the Gaussian enveloped pulse was the most stable when compared to a square form. The square form introduced numerical instabilities in the code and this combined with the very well defined blow out region and higher amplitude wake of the Gaussian enveloped pulse meant that the Gaussian was selected as the drive laser pulse form for the remaining investigation.

During the pulse length variation experimentation there were no electrons injected into the accelerating region. To remedy this an injection method which used the introduction of Nitrogen neutrals to increase the probability of having electrons trapped was proposed and investigated. The results concluded that there was a vast increase in the number of electrons reaching higher energy. While there were electrons reaching higher energies each regime had its own inherent limitations, the higher electron density had a large amount of accelerated electrons however the distance over which these electrons were gaining energy in a bunch was limited to $L_d < 1\text{mm}$. After this distance the dephasing started to really affect the beam of electrons. To increase the dephasing length the density of He was lowered so as to be closer to the resonance condition discussed in section 2. This then gave a much more coherent electron beam which showed no signs of dephasing after the same 1mm distance. There were however much fewer electrons in the higher energy band. In order to produce a coherent electron bunch with the highest energy possible a range of concentrations must be investigate to determine at which point the number of trapped electrons is at its maximum. Once this peak trapping Nitrogen concentration has been determined the pulse length should be tailored to the resonance condition. With this ideal trapping case the plasma number density should be altered and investigated to determine the density at which the acceleration length is optimal. The plasma density and pulse length parameters can be finely tuned so that the largest possible number of electrons are injected and accelerated to the largest energy for the maximum trapping Nitrogen concentration. Another route for inquiry lies in the possibility of selecting a better suited element to use for injection in the same capacity.

With the simulation of an optimised Nitrogen trapping system the next objective would be to produce a monoenergetic beam of electrons rather than the broad energy distributions achieved in this report. The broad distributions are a result of the electrons being continually injected along the laser's path. There will always be a lower energy component to the electron bunch if the electrons are continually injected, the obvious course to reduce this effect is to make use of the lack of trapping in a pure He plasma. If the system were split into two sections, the first being an injection region which could be on the order of millimeters long and the second an acceleration region of the order of centimeters. This first injection area would consist of the idealised Nitrogen neutral method discussed section 3. This would produce a high number density electron bunch and accelerate it to an energy of $100 - 200\text{MeV}$. This electron beam would then be injected into an acceleration area consisting entirely of pure Helium and this could operate in a few different ways. The first being the original laser pulse continues into the pure He plasma of the appropriate number density and this would simply have the effect of 'switching off' the injection mechanism and allow the electrons to gain energy with out extra injection up to the GeV region.

The mechanism could instead function by injecting the electron bunch into a Helium plasma of different density which could be specifically produced to accelerate the bunch produced in the trapping area. A second laser pulse would be used to form the wakefield in the pure He plasma and hence accelerate

the beam to the GeV range.

The final part of this investigation was to produce a focussing laser beam with a view to increase the diffraction limit. The focussing beam would balance against the diffraction effects of the plasma and hence allow the laser to propagate further without diffracting. The preceding sections used a collimated drive laser pulse and this produced the necessary results but this laser is still subject to diffraction effects. While the main limitation in the injection methods section (3) was the electron dephasing length once the method is further perfected the next shortest limiting factor is the diffraction limit. During the simulations the detrimental consequences of using a laser pulse which focussed much too quickly were demonstrated. The pulse formed the electron bunch very quickly but the dephasing effect was increased at the focus due to the laser being forced to occupy such a small volume and so stretching back in to the acceleration region of the plasma wake. After the focus the laser diffracted extremely quickly and this introduced further instabilities and destroyed the electron bunch. To further study this positive contributions to the acceleration length a slowly focussing pulse must be used and a method of finding the ideal angular spread for a given plasma density determined.

Combining each of the results obtained above may allow an idealised high energy electron beam to be produced. As has been demonstrated there are many factors to consider when attempting to produce the kind of high quality electron bunch usually associated with solid state accelerators using the laser wakefield interaction. With further simulation to address each of the limiting factors this may be achieved. Fine tuning the Nitrogen injection method will produce the numbers of electrons required and this bunch could then be used in a two stage wakefield accelerator, this would reduce the dephasing limitation. Finally using a slowly focussing laser to suppress the diffraction phenomena and allow for the longest limiting scale, pump depletion, to be the only limitation. The most efficient laser wakefield accelerator will only be limited by the energy contained within the driving laser pulse.

6 Appendix

6.1 Input Decks

6.1.1 Two Stream Instability

```

begin:constant
  drift_p = 2.7e-21
  temp = 0.0
  dens = 1.0e24
end:constant

begin:control
  nx = 500
  ny = 500
  npart = 1250000
  t_end = 500 * femto

  x_min = 0
  x_max = 100.0 * micron
  y_min = 0
  y_max = 100.0 * micron
end:control

begin:boundaries
  bc_x_min = periodic
  bc_x_max = periodic
  bc_y_min = periodic
  bc_y_max = periodic
end:boundaries

begin:species
  name = right
  charge = -1
  mass = 1.0
  frac = 0.5
  temp_x = temp
  drift_x = drift_p
  rho = dens
end:species

begin:species
  name = left
  charge = -1
  mass = 1.0
  frac = 0.5
  temp_x = temp
  drift_x = -drift_p
  rho = dens
end:species

begin:output
  dt_snapshot = 5 * femto
  full_dump_every = 1
#properties at particle positions

```

```

particles = always
px = always
py = always

#properties on grid
grid = always
#ex = always
#ey = always
#ez = always
#bx = always
#by = always
#bz = always
#jx = always
#ekbar = always
#mass_density = never + species
#charge_density = always
number_density = always + species
#temperature = always + species

#distribution_functions = always
end:output

```

6.1.2 Pulse Length Variation

```

begin:constant
  lambda0 = 1.0 * micron
  temp = 0.0
  dens = 1.0e24 #lab plasma density range
  c_l = 2.99792458e8 #speed of light
end:constant

begin:control
  nx = 1500
  ny = 300 #nx
  npart = 5 * nx * ny

  # final time of simulation
  t_end = 400 * femto

  # size of domain
  x_min = -30.0 * lambda0
  x_max = -x_min
  y_min = -15.0 * lambda0
  y_max = -y_min
end:control

begin:boundaries
  bc_x_min = simple_laser
  bc_x_max = simple_outflow
  bc_y_min = periodic
  bc_y_max = periodic
end:boundaries

begin:laser
  boundary = x_min
  intensity_w_cm2 = 1.0e18

```

```

lambda = lambda0
profile = gauss(y,0,5*micron)
#t_start = 0.0
#t_end = 17.0 * femto
t_profile = gauss(time,34*femto,17*femto)
end:laser

begin:species
  name = electron
  charge = -1.0
  mass = 1.0
  frac = 1.0
  temp = 0
  density = dens
  npart_per_cell = 5
end:species

begin:species
  #He ions
  name = ions
  charge = 2.0
  mass = 4.0 * 1830
  npart_per_cell = 2
  immobile = T
  density = 0.5e24
  temp = 0.0
end:species

begin>window
  move_window = T
  window_v_x = c_l
  #when pulse is centered in window
  window_start_time = (x_max - x_min)/c_l
  bc_x_min_after_move = simple_outflow
  bc_x_max_after_move = simple_outflow
end>window

begin:output
  #timesteps between output dumps
  dt_snapshot = 10.0 * femto

  # Properties on grid
  grid = always
  ex = always
  ey = always
  ez = always
  bx = always
  by = always
  bz = always
  #jx = always
  #jy = always
  #jz = always

  #particle properties
  particles = always + species
  #px = always
end:output

#py = always
number_density = always + species
#mass_density = always
charge_density = always + species
#ekbar = always + species
temperature = never
end:output

6.1.3 Nitrogen Concentration

begin:constant
  lambda0 = 0.8 * micron
  temp = 0.0
  c_l = 2.99792458e8 #speed of light
end:constant

begin:control
  nx = 1500
  ny = 300 #nx

  # final time of simulation
  t_end = 7.0e-12

  # size of domain
  x_min = -30.0 * lambda0
  x_max = -x_min
  y_min = -15.0 * lambda0
  y_max = -y_min

  #ionisation parameters
  field_ionisation = T
  use_bsi = T
  use_multiphoton = T
end:control

begin:boundaries
  bc_x_min = simple_laser
  bc_x_max = simple_outflow
  bc_y_min = open
  bc_y_max = open
end:boundaries

begin>window
  move_window = T
  window_v_x = c_l
  #when pulse is centered in window
  window_start_time = (x_max - x_min)/c_l
  bc_x_min_after_move = simple_outflow
  bc_x_max_after_move = simple_outflow
end>window

begin:laser
  boundary = x_min
  intensity_w_cm2 = 8.0e18
  lambda = lambda0
  pol = 0.0

```

```

phase = 0.0
profile = gauss(y,0,6.7*micron)
t_profile = gauss(time,36*femto,18*femto)
end:laser

begin:species
#Nitrogen neutrals
name = nitrogen
charge = 0.0
mass = 2134.72
immobile = T
ionisation_energies = (14.58*ev,29.7*ev,
47.61*ev,77.74*ev,98.23*ev,553.97*ev,
669.34*ev)
ionisation_electron_species = (N_electron,
N_electron, N_electron, N_electron,
N_electron,N_electron, N_electron)
density = 5.0e23
npart_per_cell = 2
end:species

begin:species
name = N_electron
charge = -1.0
mass = 1.0
rho = 0.0
end:species

begin:species
name = He_electron
charge = -1.0
mass = 1.0
rho = 0.0
end:species

begin:species
#He
name = Helium
charge = 0.0
mass = 4.0 * 1830
npart_per_cell = 4
immobile = T
ionisation_energies = (24.6*ev,54.4*ev)
ionisation_electron_species = (He_electron,
He_electron)
density = 0.5e25
temp = 0.0
end:species

begin:output
#timesteps between output dumps
dt_snapshot = 1.75e-12

# Properties on grid
grid = always
ex = always
ey = always
ez = always
bx = always
by = always
bz = always
#jx = always
#jy = always
#jz = always

#particle properties
particles = always + species
px = always
py = always
number_density = always + species
#mass_density = always
charge_density = always + species
ekbar = always + species
temperature = never
end:output

begin:constant
lambda0 = 1.0 * micron
temp = 0.0
#speed of light
c_l = 2.99792458e8
#peak density of He and N neutrals
dens_max = 2e24

#Beam waist diameter size
D_0 = 10 * micron

#Radius of the beam waist
w_0 = D_0 / 2.0

#Focal length of the beam
f_x = 3.14e-4

#Rayleigh length
Z_R = (pi * (w_0)^2) / lambda0
#spot size evolution
W_x = (w_0) * sqrt(1 + (f_x / Z_R)^2)

#Radius of curvature
R_c = f_x * (1 + (Z_R / f_x)^2)

#Guoy phase determination
g_phase = atan(f_x / Z_R)
end:constant

begin:control
nx = 1000
ny = 600

```

```

# final time of simulation
t_end = 4.0e-12

# size of domain
x_min = 0.0
x_max = 100.0 * lambda0
y_min = -30.0 * lambda0
y_max = -y_min

#ionisation parameters
field_ionisation = T
use_bsi = T
use_multiphoton = T
end:control

begin:boundaries
bc_x_min = simple_laser
bc_x_max = open
bc_y_min = open
bc_y_max = open
end:boundaries

begin>window
move_window = T
window_v_x = c_l
#when pulse is centered in window
window_start_time = (x_max - x_min)/c_l
bc_x_min_after_move = open
bc_x_max_after_move = open
end>window

begin:laser
boundary = x_min
intensity_w_cm2 = 8.0e18
lambda = lambda0
pol = 0.0
phase = (2.0*pi/lambda0) * (y^2/(2.0*R_c))
- g_phase
profile = gauss(y,0,W_x)
t_profile = gauss(time,52*femto,26*femto)
end:laser

begin:species
#Nitrogen neutrals
name = nitrogen
charge = 0.0
mass = 2134.72
immobile = T
ionisation_energies = (14.58*ev,29.7*ev,
47.61*ev,77.74*ev,98.23*ev,
553.97*ev,669.34*ev)
ionisation_electron_species = (N_electron,
N_electron, N_electron, N_electron,
N_electron, N_electron, N_electron)
density = 0.06 * dens_max
npart_per_cell = 2
end:species

begin:species
name = N_electron
charge = -1.0
mass = 1.0
rho = 0.0
end:species

begin:species
name = He_electron
charge = -1.0
mass = 1.0
rho = 0.0
end:species

begin:species
#He
name = Helium
charge = 0.0
mass = 4.0 * 1830
npart_per_cell = 4
immobile = T
ionisation_energies = (24.6*ev,54.4*ev)
ionisation_electron_species = (He_electron,
He_electron)
density = 0.97 * dens_max
temp = 0.0
end:species

begin:output
# number of timesteps between output dumps
dt_snapshot = 0.50e-12

# Properties on grid
grid = always
ex = always
ey = always
ez = always
bx = always
by = always
bz = always
#jx = always
#jy = always
#jz = always

#particle properties
particles = always + species
px = always
py = always
number_density = always + species
#mass_density = always
charge_density = always + species
ekbar = always + species
temperature = never
end:output

```

6.2 Tables

6.2.1 Nitrogen Trapping ($n_{He} = 5 \times 10^{18} \text{ cm}^{-3}$)

$n(N) (\text{x}10^{17} \text{ cm}^{-3})$	N (%)	Non Dephasing Bunch, 1mm		Dephasing Bunch, 1mm	
		$n_e \text{ max } (\text{x}10^{19} \text{ cm}^{-3})$	N	$n_e \text{ max } (\text{x}10^{19} \text{ cm}^{-3})$	N
0.5	1	1.821	0.988	2.114	1.235
1.0	2	1.660	1.080	3.602	2.828
1.5	3	2.077	1.398	3.431	2.530
2.0	4	2.204	1.416	3.390	2.377
2.5	5	2.213	1.599	3.363	2.442
3.0	6	2.435	1.800	3.310	2.356
3.5	7	2.706	2.079	3.377	2.374
4.0	8	2.642	1.809	3.375	2.312
4.5	9	2.883	1.884	3.375	2.410
5.0	10	2.805	2.089	3.152	2.153

Figure 54: A table of the recorded values for peak trapping these data are plotted in the results section of Injection methods 3.2, $n_{He} = 5 \times 10^{18} \text{ cm}^{-3}$.

6.2.2 $n_{He} = 5 \times 10^{18} \text{ cm}^{-3}$ Peak Energy

$n(N) (\text{x}10^{17} \text{ cm}^{-3})$	N (%)	Energy Cut Off (MeV)	Number of Electrons
0.5	1	265.0	1051
1.0	2	219.0	1111
1.5	3	197.5	1064
2.0	4	174.5	1040
2.5	5	158.0	1046
3.0	6	143.5	1119
3.5	7	139.0	1009
4.0	8	130.8	1049
4.5	9	129.3	1054
5.0	10	129.3	1109

Figure 55: The energy cut off data which is plotted in fig. 35, this table also contains the number of electrons at the cut off energy. This was taken to be the value closest to 1000.

References

- [1] E. Esarey, C. B. Schroeder & W. P. Leemans, 'Physics of Laser Driven Plasma-Based Electron Accelerators', 2009, *Reviews of Modern Physics*, 1229-1280, Vol 81, DOI: 10.1103/RevModPhys.81.1229
- [2] S. Kar, Queen's University Belfast, *Plasma Physics Lectures*, PHY4013
- [3] G. K. Batchelor, 'An Introduction to Fluid Dynamics', Cambridge University Press, p73, 1977
- [4] D. Fleisch, 'A Students Guide to Maxwell's Equations', Cambridge University Press, 2011
- [5] Plasma Parameters, Wikipedia Contributors, Wikipedia, The Free Encyclopaedia, 2017, https://en.wikipedia.org/w/index.php?title=Plasma_parameters&oldid=766300079
- [6] J. M. Dawson, 'Nonlinear Electron Oscillations in a Cold Plasma', 1959, *Phys. Rev.* 113, 383
- [7] V. Malka et al., 'Electron Acceleration by a Wake Field Forced by an Intense Ultrashort Laser Pulse', 2002, *Science*. Vol 298, 1596
- [8] E. Esarey et al., 'Basic Physics of Laser Wakefield Accelerators', *IEEE Trans. Plasma Sci.* PS-24, 252 (1996)
- [9] T. Tajima and J. M. Dawson, 'Laser Electron Accelerator', 1979, *Phys. Rev. Lett.* 43, 267
- [10] K. Bennet, C. Brady, H. Schmitz & C. Ridgers, 'Users Manual for the Epoch PIC Codes', University of Warwick
- [11] E. Esarey, B. A. Shadwick, C.B. Schroeder & W. P. Leemans, 'Nonlinear Pump Depletion and Electron Dephasing in Laser Wakefield Accelerators', 'Proceedings of the Advanced Accelerator Concepts Workshop' edited by V. Yakimenko (AIP, New York), Vol. 737, pg. 578-574
- [12] B. A. Shadwick, C. B. Schroeder & E. Esarey 'Nonlinear Laser Energy Depletion in Laser-Plasma Accelerators', 2009, *Physics of Plasmas* 16, 056704
- [13] W. Horton, T. Tajima, 'Pump Depletion in the Plasma-Beat-Wave Accelerator', 1986, *Phys. Rev.*, A 34, 4110
- [14] R. Fitzpatrick, 'Particle in Cell Codes', (2006), <http://farside.ph.utexas.edu/teaching/329/lectures/node96.html>
- [15] Wikipedia Contributors, 'Finite Difference Time Domain', wikispaces, <https://fDTD.wikispaces.com>
- [16] F. Chen, 'Introduction to Plasma Physics and Controlled Fusion', Second Edition, 1984, Plenum Press, New York
- [17] A. Pak, K. A. Marsh, S.F. Martins, W. Lu, W.B. Mori & C. Joshi, 'Injection and Trapping of Tunnel-Ionised Electrons into Laser-Produced Wakes', 2010, *Physical Review Letters*, 104, 025003, DOI: 10.1103/PhysRevLett.104.025003
- [18] C. Mainfray & C. Manus, 'Multiphoton ionization of atoms', (1991), *Rep. Prog. Phys.* 54, 1333-1372
- [19] A. Buck, M. Nicolai, K. Scmid et al, 'Real-Time Observation of Laser-Driven Electron Acceleration', *Nature Physics*, VOL 7, 543-548, July 2011
- [20] David R. Lide (ed), *CRC Handbook of Chemistry and Physics*, 84th Edition. CRC Press. Boca Raton, Florida, 2003; Section 10, Atomic, Molecular, and Optical Physics; Ionization Potentials of Atoms and Atomic Ions
- [21] Gaussianbeam.png: en:User:DrBob (Gaussianbeam.png) [GFDL (<http://www.gnu.org/copyleft/fdl.html>) or CC-BY-SA-3.0 (<http://creativecommons.org/licenses/by-sa/3.0/>)], via Wikimedia Commons

- [22] <https://www.newport.com/n/gaussian-beam-optics>
- [23] J. Greenwood, 'PHY4025 Part: 1 Ultrafast Atomic & Molecular Dynamics in Intense Laser Fields'